FLORIDA STATE UNIVERSITY

COLLEGE OF ARTS AND SCIENCES

TROPICAL EASTERLY WAVES IN THE ATLANTIC AND EAST PACIFIC FROM A MODELING AND OBSERVATIONAL PERSPECTIVE

By

CONNOR DELAUNE

A Thesis submitted to the
Department of Earth, Ocean, and Atmospheric Science
in partial fulfillment of the
requirements for the degree of
Master of Meteorology

2025

Connor DeLaune defended this thesis on March 6, 2025.
The members of the supervisory committee are:

Vasubandhu Misra
Supervising Professor

Robert Hart
Committee Member

Chelsea Nam
Committee Member

The Graduate School has reviewed and approved the above-named committee members and certifies that the thesis has been approved in accordance with university requirements.

ACKNOWLEDGMENTS

We would like to acknowledge the support of NASA grant 80NSSC22K0595 which provided us with the IMERGv7 data through NASA's Goddard Space Flight Center and PPS and the support of COAPS which provided us with the computational resources to complete this research.

TABLE OF CONTENTS

LIST OF FIGURES

ABSTRACT

Two 16-year dynamically downscaled simulations for their tropical easterly waves (TEWs) were analyzed from global reanalysis of the atmosphere and ocean over the intra-Americas Seas region, centered over Central America. TEWs were also examined across 5 different reanalysis datasets to identify possible relationships with the Central American monsoon (CAM) and West African monsoon (WAM) and variations in seasonally African Easterly Jet (AEJ) latitude and strength. In terms of modeling, two versions of a coupled ocean-atmosphere Regional Climate Model (RCM) are interpreted at a 15-km grid resolution, differing solely in their cumulus parameterization schemes. Our analysis reveals that the RCMs were able to generate TEWs in the domain even though the global atmospheric reanalysis forcing the regional models displayed very little TEW activity. There were also important differences between the two versions of the RCMs, suggesting that the cumulus parameterization scheme has an important bearing on the generation of TEW in the simulation over this region. For example, in one RCM simulation, the response of the TEW was much stronger in terms of the enhanced convective activity with both convective and stratiform precipitation associated with TEWs being higher than the other cumulus scheme used in the other RCM simulation. However, the limitations and advantages of the impacts of the two cumulus parameterization schemes on the overall TEW simulation refrain us from claiming one scheme is superior to the other. Looking at the observational analysis, correlations between the CAM onset and seasonally averaged AEJ latitude yielded the most robust relationships with TEW frequency and structure such as amplitude and relative vorticity. Environmental parameters such as low-level geopotential heights, mid-level moisture, and deep-layer bulk shear were also correlated with these variations in monsoons and the AEJ, showing statistically significant connections between the environments in and around Africa, the Atlantic, and East Pacific. In all, this study highlights the improvements made to TEW simulation through dynamical downscaling and cumulus parameterizations and establishes connections with the CAM, WAM, and AEJ to the environmental conditions TEWs propagate through along with their frequency and structure.

CHAPTER 1

INTRODUCTION

1.1 Background

Tropical easterly waves (TEWs) are westward propagating, inverted Rossby-like waves, which are ubiquitous throughout the tropics and occur year-round. A large fraction of TEWs develop over northern Africa (also referred to as African Easterly Waves) and result in downstream tropical cyclogenesis in the Atlantic with approximately 50-60% of all tropical storms and Category 1 and 2 hurricanes and 80% of major hurricanes (i.e., Category 3+) originating from TEWs (Burpee 1972; Landsea 1993; Agudelo et al. 2011). Similarly, the East Pacific has been designated as the most active tropical cyclogenesis region in terms of genesis occurrence per unit area per time, most of which are triggered by a TEW (Gray 1968; Avila and Pasch 1992; Molinari et al. 2000). TEWs also play a huge role in regional precipitation across the Atlantic and East Pacific with some regions such as the Pacific coast of Central America receiving over 50% of their May-November rainfall from TEWs (Dominguez et al. 2020). Therefore, TEWs are of immense importance to study their genesis, evolution, and variability. Generally, TEWs over western Africa and the Atlantic have a phase speed of 5-10 m/s, a period of 3-5 days, and a wavelength of approximately 2000 km (Avila and Pasch 1992). There are numerous theories on the development of TEWs: the barotropic-baroclinic instability of the African Easterly Jet (AEJ; Burpee 1972, 1974; Diaz and Aiyyer 2015), diabatic heating from convective instability leading to downshear TEW growth (Mekonnen et al. 2006; Thorncroft et al. 2008), mountain lee waves from eastern Africa evolving into TEWs (Lin et al. 2005), inertial instability from cross-equatorial pressure gradients (Toma and Webster 2010), and Intertropical Convergence Zone (ITCZ) breakdowns (Ferreira and Schubert 1997). TEWs can also locally generate in the Caribbean Sea and East Pacific through diabatic heating interacting with barotropic instability associated with unstable jets such as the Caribbean low-level jet (CLLJ) and the Papagayo jet (PJ; Rydbeck et al. 2017; Whitaker and Maloney 2020; Torres et al. 2021).

Numerous studies have used regional climate models (RCMs) to understand TEWs (e.g., Lin et al. 2005; Hsieh and Cook 2007; Seo et al. 2008; Rydbeck et al. 2017; Dominguez et al. 2020). These studies use RCMs with coarser resolutions than this study and for shorter periods of

time ranging from a case study (Lin et al. 2005; Whitaker and Maloney 2020) to several years (5-10 years) of seasonal simulations (Rydbeck et al. 2017). More recent studies have focused on the generation of TEWs in the East Pacific. For instance, Rydbeck et al. (2017) showed in an RCM that a large fraction of TEWs in the East Pacific form locally through mesoscale convective systems (MCSs) forming in the Panama Bight region west of Colombia and propagating westward over the East Pacific Warm Pool. By removing terrain over northern South America, Panama, and Costa Rica, the number of TEWs simulated in the East Pacific was reduced but not completely eliminated, suggesting that TEWs do propagate across the Atlantic into the East Pacific (Rydbeck et al. 2017). Whitaker and Maloney (2020) examined a Panama Bight MCS from June 2012 that spawned a TEW, verifying the findings of Rydbeck et al. (2017) and showing the influence of the PJ and Choco Jet on the upscale growth of these MCSs. The resolution of these RCMs is also important in simulating TEW activity as shown in Seo et al. (2008) where two coupled atmosphere-ocean RCMs with differing resolutions were analyzed over West Africa and the tropical Atlantic. They indicated that the higher atmospheric model resolution produced a more accurate precipitation climatology and seasonality through improved TEW-induced moisture convergence and convection than a coarser atmospheric model coupled with a finer ocean model. Physical parameterizations in the RCMs play a huge role in TEW generation and precipitation. Dominguez et al. (2020) ran a 24-member ensemble with varying model parameterizations to test which combination would yield the most accurate TEW climatology and seasonal rainfall percentages attributed to TEWs over the Atlantic, northern South America, Central America, and the East Pacific. They found that cloud microphysics and convective schemes had the greatest impact on TEW activity and rainfall.

In terms of identifying TEWs, many methods have been utilized to track throughout the years ranging from Hovmöller diagrams of meridional winds (Fuller and Stensrud 2000; Fink et al. 2004; Ladwig and Stensrud 2009; Agudelo et al. 2011), relative vorticity maxima (Hodges 1995; Thorncroft and Hodges 2001), total precipitable water thresholds, advection of curvature vorticity (Berry et al. 2007), and advection of curvature vorticity anomalies (Belanger et al 2017). Similar to modeling, identifying TEWs in reanalysis datasets depends heavily on the dataset selected and its resolution along with the choice of tracking technique (Belanger et al. 2017; Lawton et al. 2025). Each technique has its strengths and weaknesses from resolving

terrain-induced disturbances and computational efficiency. For example, the use of Hovmöller diagrams introduced subjectivity to the tracking method while the advection of curvature vorticity anomalies is computationally inefficient as a climatology of curvature vorticity must be established. The region of analysis is also a significant part of identifying TEWs as local climatic and geographical features can play a huge role in convection and wind shear patterns. Therefore, for this study, TEWs will be analyzed over Africa, the Atlantic, and East Pacific. These regions were selected as TEWs are influenced by the AEJ and propagate through two distinct monsoonal regions: West Africa and Central America.

1.2 Purpose of the Study

This study can be broken down into two parts: a model analysis of TEW activity over the Central American region and observational analysis of TEW activity across Africa, the Atlantic, and East Pacific in reanalysis datasets through correlation with variations in the AEJ and the onset of the Central American Monsoon (CAM) and West African Monsoon (WAM).

1.2.1 Modeling Perspective

In terms of modeling TEWs, we examine the impact of dynamical downscaling of a coarse atmospheric reanalysis using a high resolution coupled atmosphere-ocean RCM over Central America on the simulations of TEWs. Additionally, we also analyze the impact of cumulus parameterization in the RCM, like Dominguez et al. (2020), by running two separate 16-year simulations with differing cumulus parameterization schemes. The regional domain of the model includes portions of the Intra-Americas Seas and the Western Hemisphere Warm Pool (Wang and Enfield 2001). This region contains two mid-level jets at 600 mb: one around 2°N off the northwest coast of South America and another around 12-15°N in the Caribbean Sea. The CLLJ is also present in the region at 925 mb and resides around 13°N between 73°W to 95°W with peak wind speeds of 12 m/s (Amador 1998; Cook and Vizy 2010). Studies have shown that TEWs can intensify through the barotropic instability that these jets provide (Molinari et al. 2000; Serra et al. 2010; Torres et al. 2021). Recently, Torres et al. (2021) showed that easterly waves in the East Pacific can be triggered by finite-amplitude transient heating in the vicinity of the mid-level jet over the Caribbean Sea with stratiform and shallow convective latent heating profiles producing the best downstream TEW growth. Therefore, this study's use of two

convective parameterizations will show how differing latent heating profiles can generate different levels of TEW growth.

1.2.2 Observational Perspective

TEW frequency and structure are examined to identify consistency across 5 different reanalyses. The position and strength of the AEJ and the onset dates of the CAM and WAM are also correlated with the track density and structure (i.e., wavelength, amplitude, trough-averaged relative vorticity, etc.) of TEWs across these reanalysis datasets. In addition, studies such as Emanuel (2022) and Bercos-Hickey and Patricola (2025) have linked the environments which TEWs propagate through to their cyclogenesis potential rather than the strength of the TEWs, so correlations with different environmental parameters such as low-level geopotential height, mid-level moisture, and deep layer wind shear are investigated. These connections can be incorporated into seasonal forecasts of tropical cyclones (TCs) in the Atlantic and East Pacific to better prepare communities for hurricane seasons as the CAM and WAM onset dates can be determined by April and May of each hurricane season.

The RCM used in this study will be described along with the experiments conducted and the algorithm used to track the TEWs in the model outputs and reanalysis datasets in Chapter 2. The methodology behind the composites and correlations will also be discussed. In Chapter 3, the results of the model analysis and observational correlations will be examined, followed by conclusions in Chapter 4.

CHAPTER 2

DATA AND METHODOLOGY

2.1 RSM-ROMS

2.1.1 Model Setup

The RCM utilized in this study is the Regional Spectral Model-Regional Ocean Modeling System (RSM-ROMS), which has been widely used for regional climate downscaling and modeling around the world (Li et al. 2012; Ham et al. 2016; Misra et al. 2022). For this study, the RSM and ROMS components of the model are configurated to have a spatial resolution of 15 km. Since the surface discretization is identical, fluxes from the atmosphere and ocean can be exchanged at 1-hour intervals directly without the need for flux couplers or interpolations.

The RSM component is originally from Juang and Kanamitsu (1994) and has gradually undergone development over the years with the latest version used for this study detailed in Misra et al. (2022). There are 28 terrain-following sigma pressure levels reaching approximately 2 hPa, and the physics of the RSM include the following parameterizations: a non-local boundary layer scheme (Hong and Pan 1996), the four-layer community Noah land surface model (Ek et al. 2003), longwave radiation (Chou et al. 1996), shortwave radiation (Chou and Suarez 1994), shallow convection (Tiedtke 1983), prognostic clouds (Zhao and Carr 1997), gravity wave drag (Alpert et al. 1988), and deep convection schemes of Relaxed Arakawa Schubert (RAS; Moorthi and Suarez 1992) and Kain-Fritsch version 2 (KF2; Kain and Fritsch 1993).

The ROMS component is a free-surface, terrain following a primitive equation model with 30 vertically stretched terrain (S) levels with higher resolution provided in the upper 500 m of the ocean and uses the Arakawa-C grid for horizontal discretization (Haidvogel et al. 2000; Shchepetkin and McWilliams 2005). The ROMS utilizes the following physical parameterizations: a local closure scheme of 2.5 level turbulent kinetic energy (Mellor and Yamada 1982), generic length scale parameterization (Umlauf and Burchard 2003), second order biharmonic diffusion (Ezer et al. 2002), and boundary layer formulation from Large et al. (1994).

RSM-ROMS was initialized using NCEP-R2 for the atmospheric component and Simple Ocean Data Assimilation v 2.2.4 (SODA; Carton and Giese 2008) for the ocean component. The lateral boundary conditions of the model were also forced by these two datasets.

2.1.2 Model Experiments

RSM-ROMS was integrated twice over a period of 16 years (1986-2001). In one version of RSM-ROMS, we use the RAS convection scheme, referred to as RR-RAS, and in the other, we use the KF2 convection scheme, hereafter referred to as RR-KF2. Given earlier discussion of the importance of diabatic heating in the simulations of TEWs, we selected these 2 deep convection schemes as they are extensively used in climate modeling studies (e.g., Ham and Hong 2013, He et al. 2015, Peishu et al. 2017). These schemes differ in concept with RAS based on quasi-equilibrium theory of convection acting to maintain equilibrium with the generation of available energy from large-scale processes while KF2 triggers convection when a certain criterion of instability and moisture availability is met. The implementation of the schemes was quite different as well. Clouds in RAS are represented by a spectrum of cloud types with detrainment level at varying pressure levels while a single-column convective cloud model is utilized in the KF2 scheme. This will greatly impact the dynamical structures of TEWs tracked along with the amount of precipitation they produce.

2.2 DATA

2.2.1 Wind and Tropical Easterly Waves

We decided to utilize the Belanger et al. (2017) objective algorithm due to the use of curvature vorticity anomalies which allow for TEWs to be tracked based on variations in the background curvature vorticity fields rather than a single vorticity threshold.

The algorithm obtained from Belanger et al. (2017) tracks TEWs based on curvature vorticity advection; therefore, the only data required for the algorithm is U and V wind components at a desired pressure level, which for our study is 600, 700, and 850 mb. The algorithm was applied to RR-RAS and RR-KF2, the European Centre for Medium-Range Weather Forecasts (ECMWF) Reanalysis v5 (ERA5; Hersbach et al. 2020), and National Center for Environmental Prediction-Department of Energy Reanalysis II (NCEP R2; Kanamitsu et al.

2002). Other TEWs were identified using the Climate Forecast System-Reanalysis (CFS-R; Saha et al. 2010), NCEP/National Center for Atmospheric Research Reanalysis I (NCEP-NCAR; Kalnay et al. 1996), ECMWF Reanalysis-Interim (ERA-Interim; Dee et al. 2011), and ECMWF Reanalysis-40 (ERA-40; Uppala et al. 2005) using the algorithm from Belanger et al. (2017) and are available via the National Center for Environmental Information (NCEI) African Easterly Wave Climatology, Version 1. The years analyzed along with the resolution of the datasets are provided in Table 1.

Table 1: Spatial and temporal resolution and period of analysis for each dataset

Dataset	Spatial Resolution	Temporal Resolution	Period of Analysis	Reference
RR-RAS	15km x 15km	6 hourly	1986-2001	Misra et al. (2022)
RR-KF2	15km x 15km	6 hourly	1986-2001	Misra et al. (2022)
ERA5	0.25° x 0.25°	6 hourly	1986-2022	Hersbach et al. (2020)
NCEP R2	2.5° x 2.5°	6 hourly	1986-2001	Kanamitsu et al. (2002)
CFS-R	0.5° x 0.5°	6 hourly	1979-2010	Saha et al. (2010)
NCEP-NCAR	210km x 210km	6 hourly	1974-2010	Kalnay et al. (1996)
ERA-Interim	1° x1°	6 hourly	1979-2010	Dee et al. (2011)
ERA-40	120km x 120km	6 hourly	1965-2001	Uppala et al. (2005)

925 mb winds were also utilized in RR-RAS, RR-KF2, ERA5, and NCEP R2 to calculate wind anomalies from 1986-2001 to examine the different low-level jets in the Central American region.

2.2.2 Precipitation

The Climate Hazards Group InfraRed Precipitation with Station data (CHIRPS; Funk et al. 2015) v2.0 was analyzed from 1981-2023 to determine the onset dates of the WAM and CAM (specifically over Panama, Costa Rica, and Nicaragua) using the cumulative rainfall anomaly technique (Liebmann and Marengo 2001; Misra and DiNapoli 2014). CHIRPS uses in-situ rain gauge interpolated with the CHPclim 0.05° resolution satellite imagery to create a rainfall dataset

between 50°S-50°N (Funk et al. 2015). This dataset was chosen over others due to its incorporation of in-situ measurements and greatest temporal overlap with the reanalysis looked at in this study.

For comparisons with RR-RAS and RR-KF2, the National Aeronautics and Space Administration's (NASA) Integrated Multi-Satellite Retrievals for Global Precipitation Mission version 7 (IMERGv7) rainfall data was utilized. This dataset uses an algorithm to combine NASA's Tropical Rainfall Measurement Mission (TRMM) satellite measurements from 2000-2015 with the new NASA's Global Precipitation Mission (GPM) measurements from 2014-present. The rainfall data is available at a spatial resolution of 0.1° with a temporal resolution of 30 minutes. Due to computational limitations, the IMERGv7 resolution was lowered to 0.25° and averaged to 6-hourly means to match the temporal resolution of the TEW datasets.

Unlike IMERGv7 though, RR-RAS and RR-KF2 separates convective precipitation from total precipitation, and using the difference between total and convective rainfall, stratiform precipitation can be extrapolated from the model data as well. Therefore, the TEWs can be analyzed in terms of convective versus stratiform precipitation which can have implications on the heat profiles observed in the model simulations. Precipitation rates in the models were also linearly interpolated to 0.25° to match the spatial resolution of IMERGv7.

2.2.3 Other Climate Variables

Additional variables from ERA5 such as 850 mb geopotential height, 700 mb relative humidity, and 200-850 mb bulk wind shear were correlated with the onset dates of the CAM and WAM along with the latitude and strength of the AEJ. This allows for environmental teleconnections to be established that could impact TEW tracks and structures along with cyclogenesis from TEWs (Emanuel 2022; Bercos-Hickey and Patricola 2025).

2.3 METHODOLOGY

2.3.1 Tropical Easterly Wave Tracking and Analysis

As stated earlier, an objective "trough" tracking algorithm from Belanger et al. (2017) was used to identify TEWs in RR-RAS, RR-KF2, ERA5, and NCEP R2 at 600 mb, 700 mb, and 850 mb and is shown in Fig. 1. The algorithm uses the advection of curvature vorticity on a 2-D

wind field to track TEWs through a 4-step process. The first step is shown in Fig. 1a where a 2-D wind field is inputted. Shear, curvature, and relative vorticity are calculated for all years of analysis, and a climatology of curvature vorticity is created. In step 2, the curvature vorticity anomalies are calculated and smoothed through a 9-point Gaussian filter. TEWs are then identified in regions where the curvature vorticity anomalies exceeded the 70th percentile of the curvature vorticity climatology, the zonal wind is less than 2.5 m/s, and the advection of curvature vorticity anomalies is 0 s^{-2}.

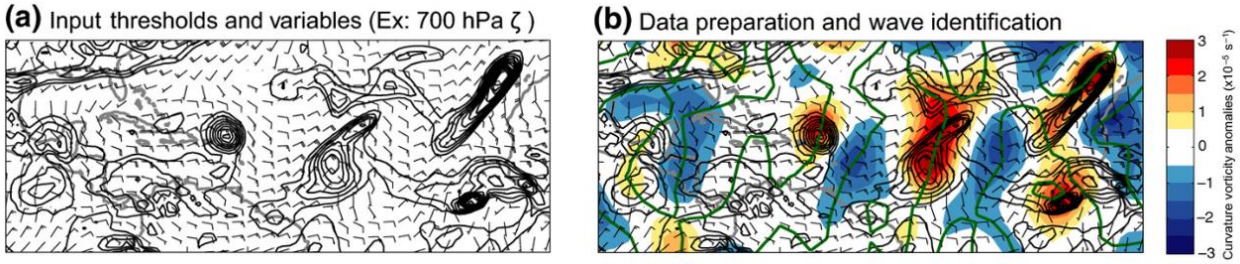

Figure 1: A schematic of the objective algorithm used to track tropical easterly waves from Belanger et al. (2017). (a) 700 hPa wind field for 15 August 2008 at 00z with 700 hPa relative vorticity contoured for regions greater than 0 s^{-1}. (b) 700 hPa curvature vorticity anomalies are contoured in color with the green contour showing regions where the advection of curvature vorticity anomalies is equal to 0^{-2}.

After all TEWs are identified, in part 3, trough axes are merged together depending on the overlap in curvature vorticity anomalies near TEW endpoints as seen transitioning from Fig. 1c to Fig. 1d. The final step consists of removing any TEWs that did not last at least 2 days and had median propagation speeds outside -25 m/s to -2 m/s. For this study, TEWs were identified from 1986-2022 in ERA5 between 0°-30°N and 110°W-30°E and only for 1986-2001 in RR-RAS, RR-KF2, and NCEP-R2 between 5°S-25°N and 100°W-70°W. It is also important to note that the 70th percentile of curvature vorticity climatology differs from Belanger et al. (2017) where the 66th percentile of curvature vorticity anomalies were utilized. This was due to computational issues loading in all the curvature vorticity anomalies across the 37 years analyzed in ERA5, and the 70th percentile ensured no negative threshold were utilized. A comparison of the two thresholds over shorter time periods yielded similar track densities. In addition, since this method was applied to RR-RAS, RR-KF2, ERA5, and NCEP-R2, the comparisons in TEW activity are still valid.

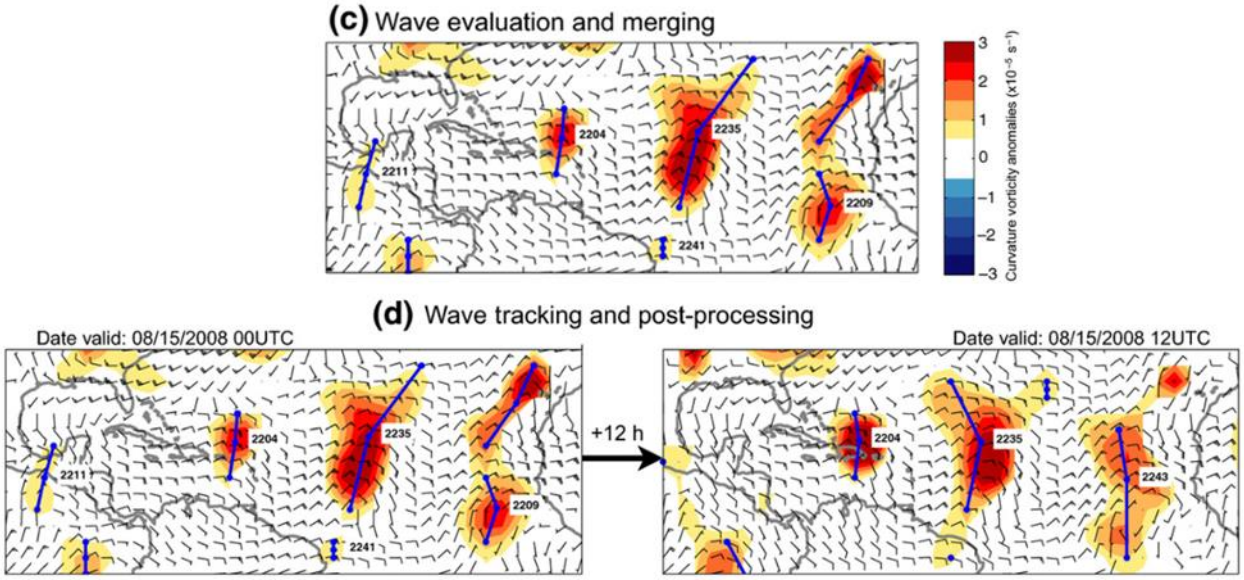

Figure 1 (cont.): (c) Curvature vorticity anomalies that exceed the threshold (5e-06 s^{-1} in this case) are shaded with tropical easterly wave troughs denoted by blue lines. (d) Tropical easterly wave trough progression after 12 hours from (c), valid for 15 August 2008 at 12z.

Track densities for each dataset and pressure level were analyzed using the 6-hourly centroid point of each TEW axis and calculated using the frequency of points in a 2° box. TEW wavelengths were calculated using a function from Belanger et al. (2017) which used a factor four scale to measure the TEW zonal extent based on the direction of the TEW propagation, and TEW amplitudes were computed using the distance between the wave centroid location and the northern most point. 925 hPa wind anomalies were also analyzed by extracting all the anomalies when TEWs were present in the Central American model domain (i.e., between 1°N-21°N and 96°W-72°W) and compositing them together. To analyze TEW vorticity, a 5° box was utilized around the wave centroid point to calculate the areal relative vorticity before being averaged across the entire TEW lifespan. A 5° box was selected to ensure that just the wave trough was being incorporated into the calculations. Since the TEW datasets from the NCEI included mean trough-averaged relative vorticity, those were averaged across the TEW lifespan. To make this study more robust, only the TEWs that exceeded an average areal vorticity of 0 s^{-1} were analyzed in Chapter 4.1 when comparing the TEW performance in RR-RAS and RR-KF2 due to the areal vorticities being lower in the model than the reanalysis. In Chapter 4.2, unfiltered TEWs were examined along with filtered TEW track densities that removed TEWs with average areal vorticities of 1e-5 s^{-1}. For the TEW precipitation analysis, a 10° box around each centroid point

was utilized to attribute precipitation to TEWs. Similar studies vary between what distance to attribute precipitation around a TEW axis with Dominguez et al. (2020) utilizing a 15° box based on the findings of Agudelo et al. (2011) and Hollis et al. (2024) using a 500 km radius around the wave center, so a consensus was applied in this study.

2.3.2 Correlations

Correlation coefficients were calculated for TEW track densities, wavelengths, amplitudes, and areal averaged relative vorticities using the CAM and WAM onset dates calculated via CHIRPS and the seasonally averaged AEJ latitude and maximum zonal wind speed averaged over each May-November season from 1981-2023. To better visualize the differences in TEW structures between datasets, these correlations were made with probability density functions of the TEW wavelengths, amplitudes, and areal averaged relative vorticities normalized for each reanalysis based on their maximum probability of occurrence. This ensures comparisons are consistent as wavelengths, amplitudes, and vorticities vary across datasets and differing spatial resolutions.

The statistical significance of these correlations was determined using a p-value test where p-values less than 0.05 represent 95% significance. Other correlations between ERA5 850 mb geopotential height, 700 mb relative humidity, and 200-850 bulk shear with the monsoon onsets and AEJ variations were also calculated and used the same significance testing.

CHAPTER 3

RESULTS

The results of this study will be divided into 2 sections covering the analysis of the model simulations and the observations.

3.1 Impact of Dynamical Downscaling on Tropical Easterly Waves

In this section, TEW track densities, wavelengths, amplitudes, and average areal relative vorticities in RR-RAS, RR-KF2, ERA5, and NCEP R2 will be discussed along with 925 mb wind anomalies when TEWs are present in the Central America model domain and May-November precipitation percentages attributed to TEWs.

3.1.1 Climatological Track Densities

We show in Fig. 2 the climatological frequency of TEWs at 600 hPa for May-November which incorporates the North Atlantic and East Pacific tropical cyclone seasons. ERA5 which is used as a validation dataset in Fig. 2a shows the highest frequency of TEWs at 10+ per year in the Panama Bight region and a broader region of more moderate activity (2-8 per year) across the domain on either side of the Central American isthmus. The NCEP R2 reanalysis in Fig. 2b conversely shows marginal TEW activity with a frequency of less than 2 per year across most of the domain. NCEP R2 also lacks TEWs around the ITCZ in the East Pacific where the maxima in ERA5 were located, indicating that the low resolution of NCEP R2 may have prevented the local generation of TEWs discussed in Rydbeck et al. (2017) and Whitaker and Maloney (2020). The downscaling of NCEP R2 in RR-RAS and RR-KF2 substantially increases the TEW activity (Fig. 2c,d), especially along the Pacific slope of Central America. In RR-RAS, the TEW frequency is 4-6 per year, while along the Caribbean coast it is ≤ 4 per year. In the RR-KF2 simulation, the count of TEWs is well over 10 per year along the Pacific coast of Central America, while along the Caribbean coast it is ≥ 6 per year. Even though the more convective-allowing RR-KF2 produced more TEWs, neither model runs were able to reproduce the TEW activity along the East Pacific ITCZ seen in ERA5. However, RR-RAS has a cold SST bias along the coastal oceans (not shown) which can produce weaker convection along the Pacific coast of Central America and less TEWs. This cold bias is improved in RR-KF2, allowing for more

generation of TEWs, but does not explain the lack of high TEWs over the open oceans. Another critical bias in both model simulations is terrestrial rain with higher rainfall amounts being generated over the Pacific slope of Central America than what is seen in IMERGv7 (not shown). This pulls the average ITCZ location in RR-RAS and RR-KF2 further north than what is observed in ERA5.

Regardless, dynamical downscaling in RR-RAS and RR-KF2 did allow for in situ TEWs to form in the East Pacific compared to NCEP R2. By increasing the resolution, terrain-induced convection and gradients such as wind speed and temperature can be improved in the model simulations, allowing for more accurate representations of regional jets and instability. For example, not shown, NCEP R2 struggled in producing the negative potential vorticity gradient (i.e., barotropic instability) in the East Pacific between 2-4°N seen Torres et al. (2021) while it is present in ERA5, RR-RAS, and RR-KF2. This suggested that the present of barotropic instability near the Panama Bight is needed for downshear TEW growth from MCSs in the region.

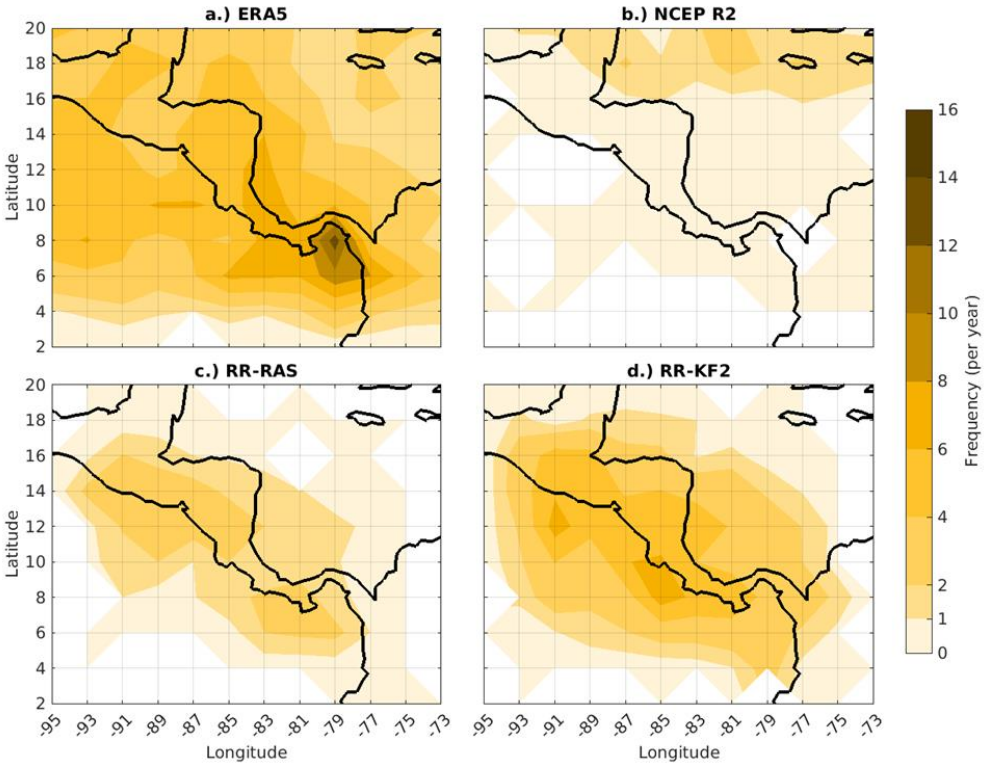

Figure 2: May-November average TEW track density at 600 hPa for (a) ERA5, (b) NCEP R2, (c) RR-RAS, and (d) RR-KF2 for 1986-2001.

Fig. 3a shows the climatological frequency of TEWs at 700 hPa with maximum TEW frequency along Colombia's Pacific coast and in the mid-ocean over northeastern Pacific along 6°N latitude in ERA5. This TEW activity in ERA5 close to the equator appears to be associated with the secondary mid-level jet around 2°N mentioned in Torres et al. (2021), providing a source of barotropic instability, and the seasonally averaged location of the ITCZ. Like at 600 hPa, RR-RAS enhances TEW activity around Central America (Fig. 3c) and is further enhanced in RR-KF2 (Fig. 3d). However, the activity at 700 hPa in the model runs is slightly lower than what was observed at 600 hPa while activity in ERA5 increased slightly. The spatial pattern of the frequency of TEWs in both RR-RAS and RR-KF2 are aligned with the Central American isthmus, with RR-KF2 showing greater activity over the isthmus and along the Pacific coast of Nicaragua and El Salvador, near the exit region of the PJ. Again, this reinforces the northern ITCZ bias present in the model simulations.

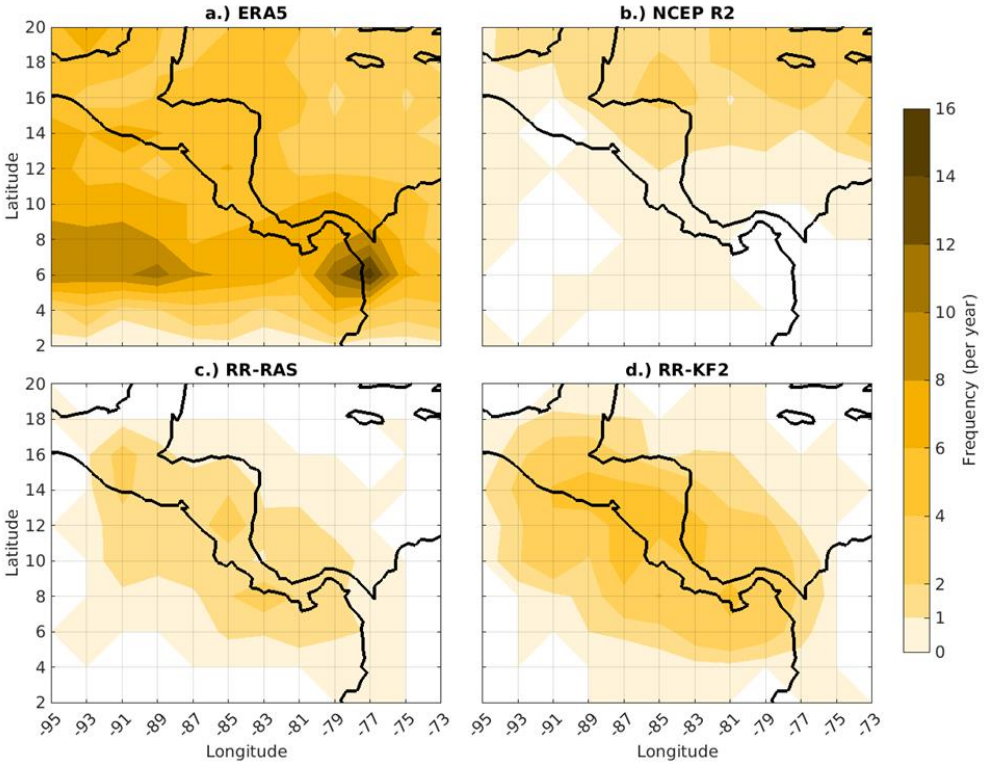

Figure 3: May-November average TEW track density at 700 hPa for (a) ERA5, (b) NCEP R2, (c) RR-RAS, and (d) RR-KF2 for 1986-2001.

At 850 hPa, the Atlantic coast of Panama and Colombia show high TEW activity around 11°N (in the vicinity of the CLLJ) extending to the southwest where a maximum of 26-30 TEWs

per year occur in Panama Bight region. Interestingly, ERA5 has another local maximum in TEW activity further north of 18°N in (Fig. 4a). On the other hand, NCEP R2 continues to show insignificant TEW activity (Fig. 4b). However, only RR-KF2 (Fig. 4d) shows higher activity than NCEP R2, especially in the proximity of PJ across the Costa Rica-Nicaragua region, while RR-RAS (Fig. 4c) produced a similar number of TEWs to NCEP R2.

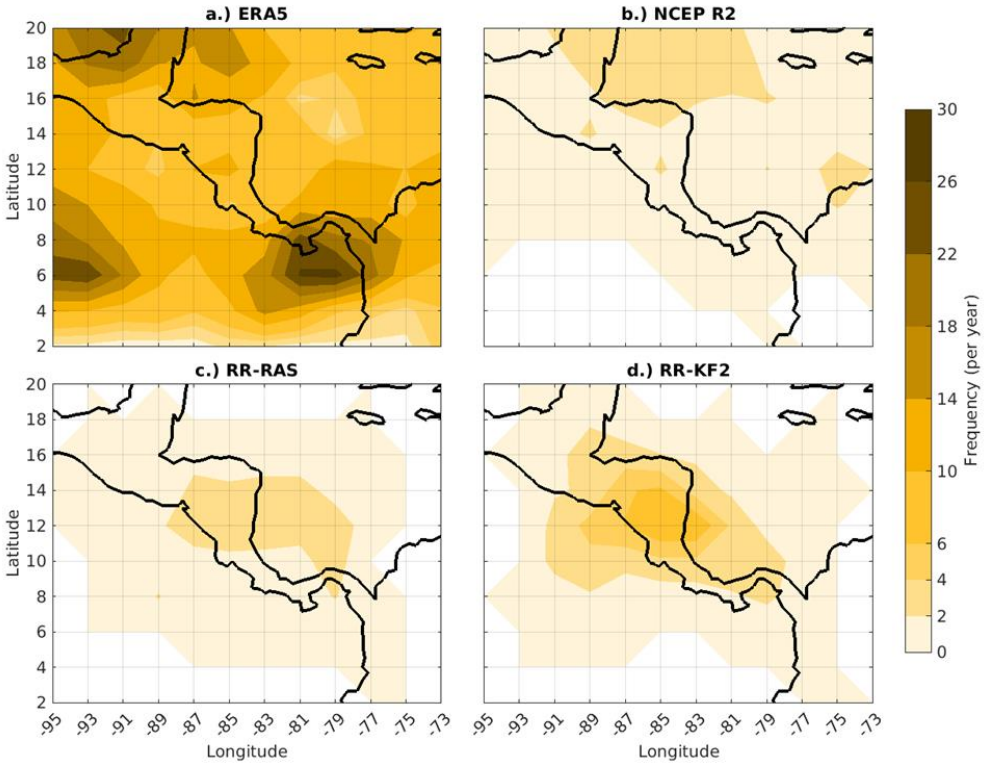

Figure 4: May-November average TEW track density at 850 hPa for (a) ERA5, (b) NCEP R2, (c) RR-RAS, and (d) RR-KF2 for 1986-2001.

Overall, from these figures, it is noticeable that the regional models can develop TEWs in the domain when the large-scale forcing from NCEP R2 had barely any such activity, suggesting the potential for local generation of these waves (Rydbeck et al. 2017; Whitaker and Maloney 2020; Torres et al. 2021). It is important to note that neither RR-RAS nor RR-KF2 replicated the Caribbean TEW activity around 18°N found in NCEP R2. Furthermore, the regional models are unable to reproduce the comparatively high density of these TEWs in the Panama Bight region found in ERA5. This was an unrealistic outcome though as NCEP R2, used to initialize the model, lacked TEW activity in the East Pacific, so RR-RAS and RR-KF2 had to generate its own

TEWs through the barotropic instability enhanced by the higher resolution gradient in zonal wind speeds in the low-to-mid-levels.

3.1.2 Wavelengths

The average probability distribution of wavelength of the TEWs at 600 hPa, 700 hPa, and 850 hPa are shown in Fig. 5. Notably, ERA5 displays TEWs with wavelengths of approximately 1700 km having the most probability at all three pressure levels while the wavelengths in NCEP R2 with the highest probability are between 2500-3000 km. However, NCEP R2 shows a wider distribution of TEW wavelengths compared to ERA5 at all pressure levels. In comparison, RR-RAS and RR-KF2 show a shorter wavelength of TEWs of ~ 1300 km and ~1400 km with the highest likelihood, respectively. At 850 hPa, RR-RAS and RR-KF2 perform similarly. However, with decreasing pressure levels, RR-KF2 produces slightly wider wavelengths, closer to what is observed in ERA5. Both model simulations have narrower distributions compared to the reanalysis datasets though, indicating that RR-RAS and RR-KF2 struggle to capture the variance in TEW structure seen in reanalyses.

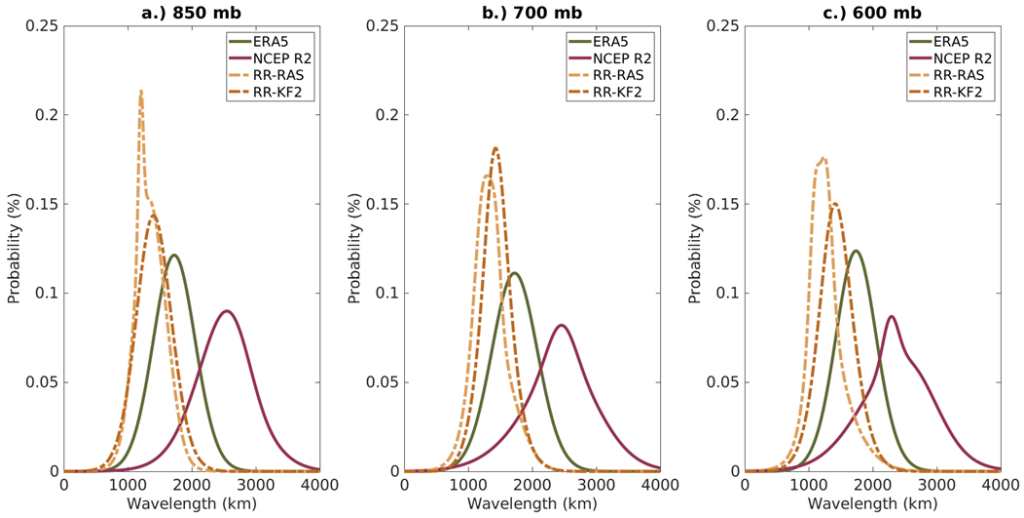

Figure 5: Probability density function of May-November TEW average wavelengths at a) 850 hPa, b) 700 hPa, and c) 600 hPa for 1986-2001. The ordinate represents the probability of the waves of a specific wavelength across the spectrum of wavelengths of the TEWs in the dataset.

Overall, Fig. 5 suggests that the regional models tend to produce TEWs with shorter wavelengths more regularly than the global reanalysis of ERA5 and NCEP R2, which displays a broader distribution of wavelengths. It is important to note though that the measurement of TEW

wavelength is dependent upon the spatial resolution of the dataset analysis as the curvature vorticity anomalies are utilized in the calculations.

3.1.3 Amplitudes

The average probability distribution of the amplitudes of the TEWs are shown in Fig. 6a-c for the three pressure levels. ERA5 displays higher amplitude TEWs with a higher probability than RR-RAS, RR-KF2, and NCEP R2 at all three pressure levels. Again, the model simulations have a narrower distribution than the reanalysis, not capturing the variations in TEW structures. Interestingly, at 850 hPa and 700 hPa, RR-RAS and RR-KF2 have the same amplitude of maximum probability as NCEP R2, around 850 km. At 600 hPa though, the regional models produced distributions with higher average amplitudes than at 850 hPa and 700 hPa but still tend to underestimate higher amplitude and overestimate lower amplitude TEWs when compared to ERA5. Regardless, this is an improvement in TEW amplitudes produced through dynamical downscaling.

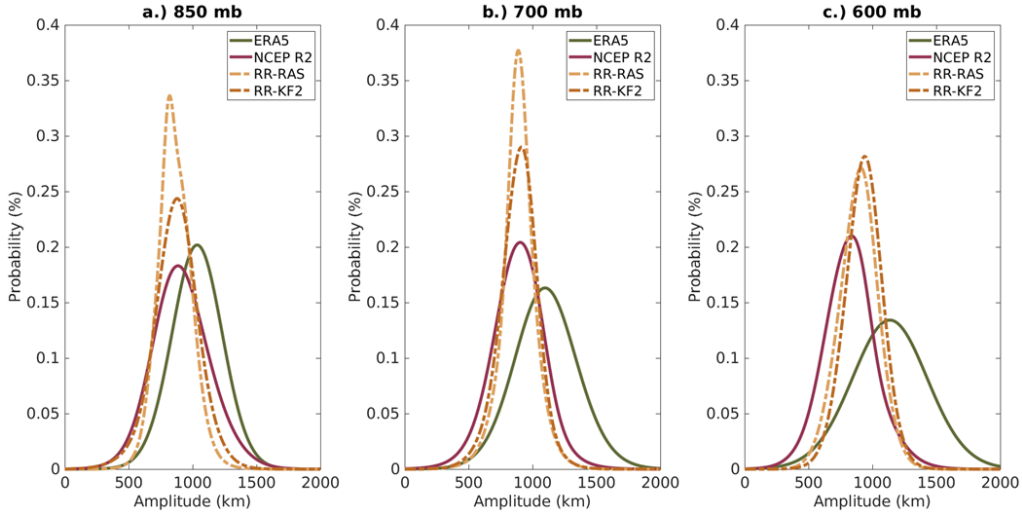

Figure 6: Probability density function of May-November TEW average amplitudes at a) 850 hPa, b) 700 hPa, and c) 600 hPa for 1986-2001. The ordinate represents the probability of the waves of specific amplitude across the spectrum of amplitudes of the TEWs in the dataset.

3.1.4 Low-level Wind Anomalies

In Fig. 7, the composite of the climatological 925 hPa wind anomalies when TEWs are present within the model domain at 600 hPa are shown. It is apparent from this figure that the

Central American monsoon gyre is reinforced by mid-level TEWs in the reanalysis datasets and regional models. However, the magnitude of the wind anomalies and the center of the gyre differs as sample sizes between datasets vary. For instance, in ERA5, the center of the gyre is located around 16°N and 93°W (Fig. 7a) while in NCEP R2 the location is slightly to the east around 89°W (Fig. 7b). Furthermore, in NCEP R2, the southern flank of the gyre shows more extensive and stronger wind anomalies than ERA5. Like the wavelength calculations, the difference in spatial resolution between ERA5 and NCEP R2 can influence the expanse and strength of the Central American gyre. Pivoting to the models, the wind anomalies are more intense on the eastward flank of the gyre in RR-RAS (Fig. 7c) compared to RR-KF2 (Fig. 7d). Spatially though, RR-KF2 places the gyre location closer to what is observed in the reanalysis.

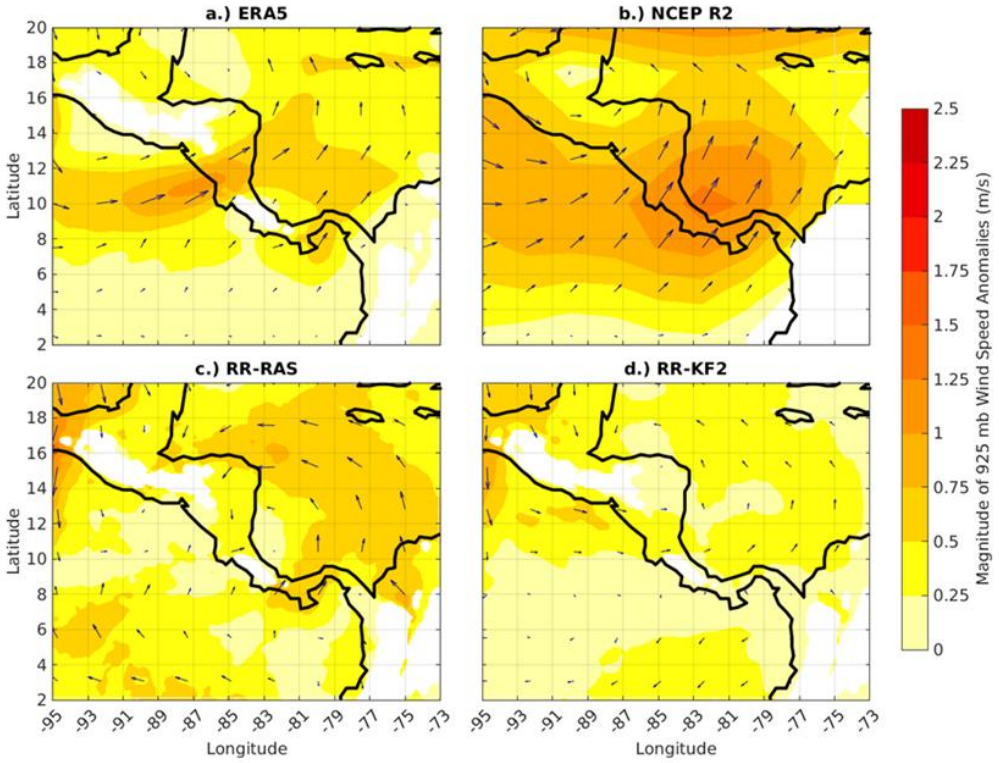

Figure 7: Average 925hPa wind anomalies (m/s) when TEWs are present in the regional model domain at 600hPa in a) ERA-5, b) NCEP-R2, c) RR-RAS, and d) RR-KF2 during May-November from 1986-2001.

Qualitatively, similar figures are obtained for wind anomaly composites at 925 hPa based on TEWs at 850 hPa and 700 hPa (not shown). Interestingly, when TEWs are present at 850 hPa in RR-RAS and RR-KF2, the PJ is 1.5-2.5 m/s stronger across Central America and into the East

Pacific. This is not seen in the reanalysis datasets. The ERA5 925 hPa anomalies were roughly 0 m/s in the PJ while NCEP R2 has a weaker PJ of 1-1.5 m/s, completely opposite of the regional models. One of the reasons for this could be the northward location of the higher track density of TEWs in model simulations compared to ERA5 (cf. Fig. 4) which could lead to stronger height gradients across the Central American isthmus near the surface. It should be noted that several studies have suggested that interactions of the TEWs with monsoon troughs can lead to cyclogenesis, so modeling this gyre is of great importance (McBride and Zehr 1981; Molinari et al. 2000). Another reason could just be high resolution of the model simulations. The PJ has a meridional extent of approximately 2.5° which would permit only one point in NCEP R2 to capture the PJ while RSM-ROMS could simulate 18-19 points meridionally along the PJ. This can allow for an accurate depiction of wind speed gradients in the region, impacting the local vorticity budget and convection.

3.1.5 Areal Relative Vorticity

In Fig. 8, we show the distribution of the relative vorticity in the trough axis of the TEW detected at 600 hPa, 700 hPa, and 850 hPa.

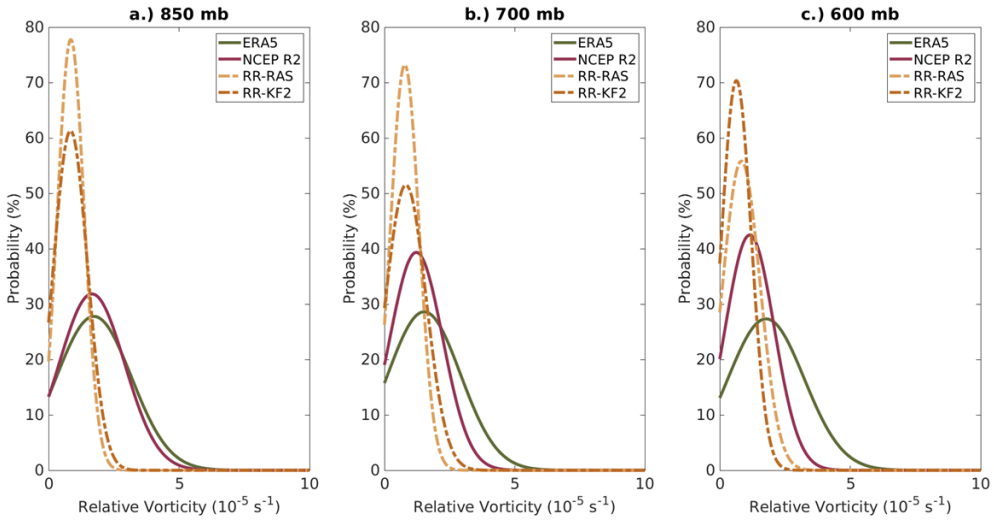

Figure 8: Probability density function of May-November TEW trough-averaged relative vorticity at a) 850 hPa, b) 700 hPa, and c) 600 hPa for 1986-2001. The ordinate represents the probability of the vorticity across the spectrum of vorticity in all the troughs of the TEWs in the dataset.

The distribution of vorticity is wider in ERA5 than what is found in NCEP R2 and the model simulations, especially at 600 hPa and 700 hPa. The NCEP R2 shows a comparable

distribution to ERA5 at 850 hPa, although the distribution is narrower in the mid-levels. Both RR-RAS and RR-KF2 display a far narrower distribution, favoring weaker vorticity values, than what is seen in ERA5 or NCEP R2. Furthermore, between the models, RR-RAS shows a slightly larger spread at 600 hPa while RR-KF2 displays a wider distribution of vorticity at 700 hPa and 850 hPa. Overall, the regional models severely underestimate the average areal vorticity of TEWs when compared to the reanalyses. These distributions are consistent with the shorter wavelengths and amplitudes of the simulated TEWs compared to ERA5 shown earlier and weaker precipitation response discussed in the following sub-section. Physically, these findings make sense due to the methods used to calculate the areal relative vorticity favoring TEWs that are more amplified and extend further zonally (i.e., longer wavelengths).

3.1.6 Precipitation Attributed to Tropical Easterly Waves

Fig. 9 shows the percentage of total precipitation (P) from TEWs at 600 hPa (computed by summing all precipitation observed within a 10° box around a TEW centroid point and dividing by the total precipitation across all May-November seasons) for ERA5, RR-RAS, and RR-KF2, respectively. In Fig. 9a, ERA5 displays the largest precipitation contribution from TEWs followed by that in RR-KF2 (Fig. 9b) and the least in RR-RAS (Fig. 9c). Even though RR-KF2 produces the same seasonal percentage as ERA5 across Nicaragua at 10-15%, the regional model severely underperforms observations, especially in the Caribbean Sea and in the East Pacific around 3-7°N.

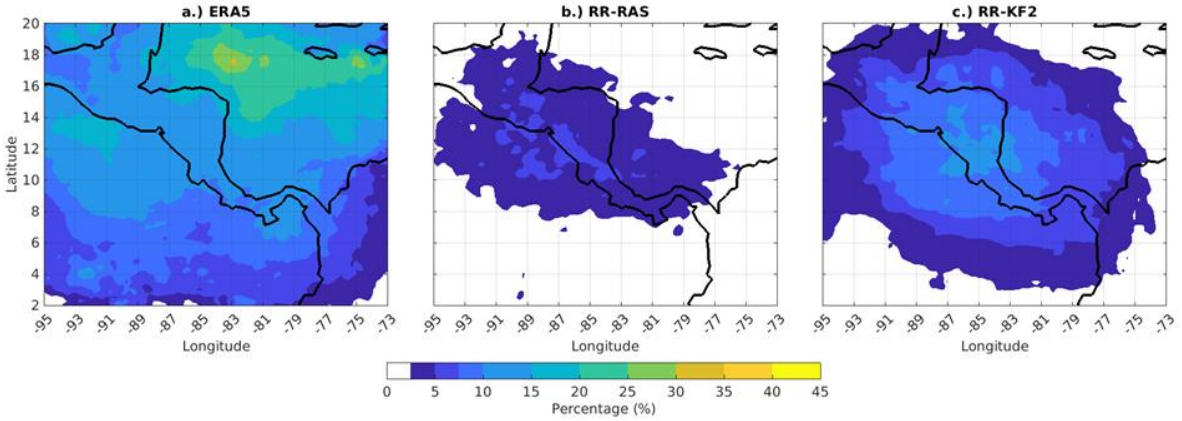

Figure 9: Percentage of May-November total precipitation attributed to TEWs present at 600hPa in a) ERA-5, b) RR-RAS, and c) RR-KF2. ERA5 uses IMERGv7 data from 2001-2022, and RR-RAS and RR-KF2 use model output rain rates from 1986-2001.

A possible reason for this discrepancy between model simulations is the difference in convective precipitation rates. In further analyzing these contributions to total precipitation from the simulated TEWs, Fig. 10 shows the corresponding contribution of the convective (CP) and stratiform (SP) precipitation between the two models. Surprisingly, the contributions from both convective and stratiform precipitation in RR-KF2 are higher than in RR-RAS, indicating that RR-KF2 produces more rainfall overall attributed to TEWs, not just convective precipitation.

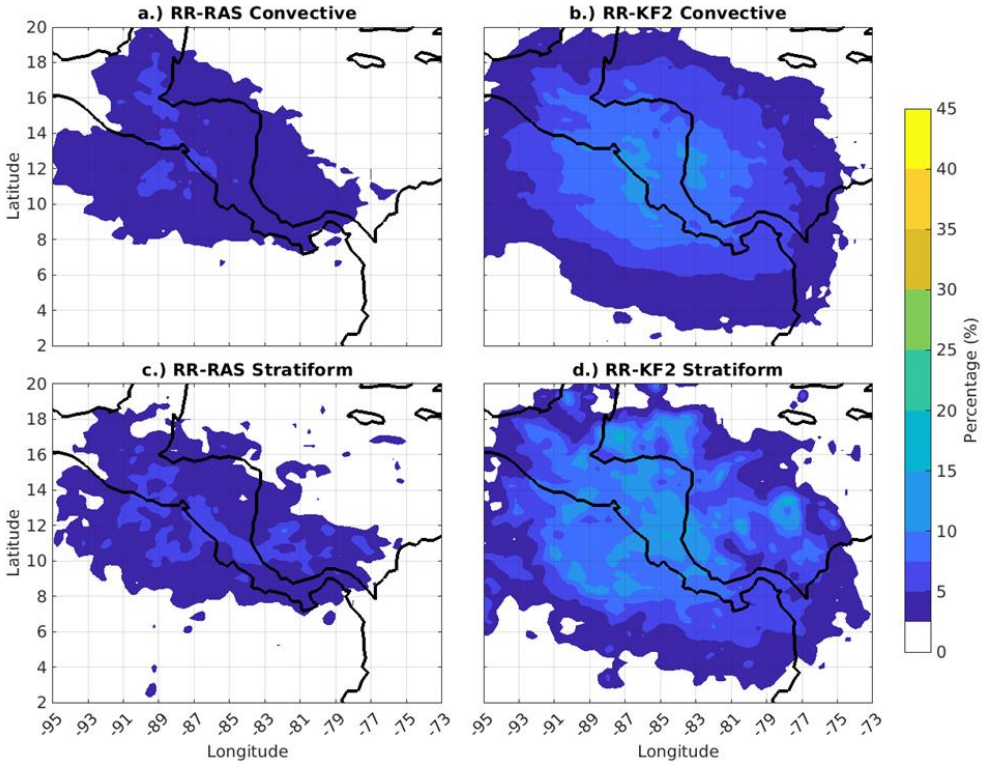

Figure 10: Percentage of May-November (a, b) convective and (c, d) stratiform precipitation attributed to TEWs present at 600 hPa in (a, c) RR-RAS, and (b, d) RR-KF2. RR-RAS and RR-KF2 use model output rain rates from 1986-2001.

These results further explain the stronger response of in situ generation of TEWs in RR-KF2 compared to RR-RAS. Several earlier studies have indicated a coherent relationship between TEW activity and convection, which leads to some regions being preferred for TEW generation and cyclogenesis (Carlson 1969; Reed et al. 1977, Fink and Reiner 2003; Kiladis et al. 2006; Mekonnen et al. 2006; Thorncroft et al. 2008; Torres et al. 2021). Additionally, Torres et al. (2021) show that the in-situ generation of TEWs is very sensitive to the vertical profile of latent heating, with the heating associated with stratiform precipitation generating the strongest

response of TEW activity in the intra-Americas region followed by shallow convection then deep convection. Fig. 10 appears to be consistent with these findings, with RR-KF2 showing higher TEW activity and percentages of seasonal stratiform rainfall attributed to TEWs than RR-RAS. Similar seasonal precipitation percentage figures were produced for 700 hPa and 850 hPa along with the convective and stratiform percentages in the model simulations, and the results were similar across pressure levels with RR-KF2 outperforming RR-RAS. Overall, the regional models failed to come close to percentages seen in ERA5 and IMERGv7, expect over Nicaragua in RR-KF2. Again, this continues to show the difficulties that the regional models have with resolving marine precipitation and TEW activity. Precipitation analysis using NCEP R2 were not produced, but the lack of TEW in the East Pacific would have yielded similar results to what is seen in RR-RAS and RR-KF2, showing the limitations of dynamical downscaling on precipitation attributed to TEWs.

3.2 Influence of the African Easterly Jet and Monsoons on Tropical Easterly Waves

This next section covers how TEWs in different reanalyses are impacted by the CAM and WAM onset dates and variations in the seasonal AEJ latitude and strength. Different environmental variables are also analyzed to determine teleconnections with these monsoonal and AEJ variations.

3.2.1 Climatological Track Densities across Reanalyses

Fig. 11 shows the climatological frequency of TEWs at 700 hPa for May-November in ERA5 (Fig. 11a), CFS-R (Fig. 11b), ERA-Interim (Fig. 11c), ERA-40 (Fig. 11d), and NCEP-NCAR. These frequencies are not filtered like the ones presented in Chapter 4.1. Across the reanalysis datasets, there is consensus of TEWs originating around 20°W and propagating across northern Africa and into the Atlantic where all datasets have a local maximum in activity near the west coast of Africa. ERA5 is an outliner in terms of this West Africa maximum and the northern track of TEWs over Africa when compared to the other reanalyses. Looking at the East Pacific, the ITCZ appears to be active in terms of TEWs across all datasets besides NCEP-NCAR which was also seen in NCEP R2 in Chapter 4.1.1. Interestingly, only the ECMWF reanalyses have another peak in frequency in the Panama Bight region.

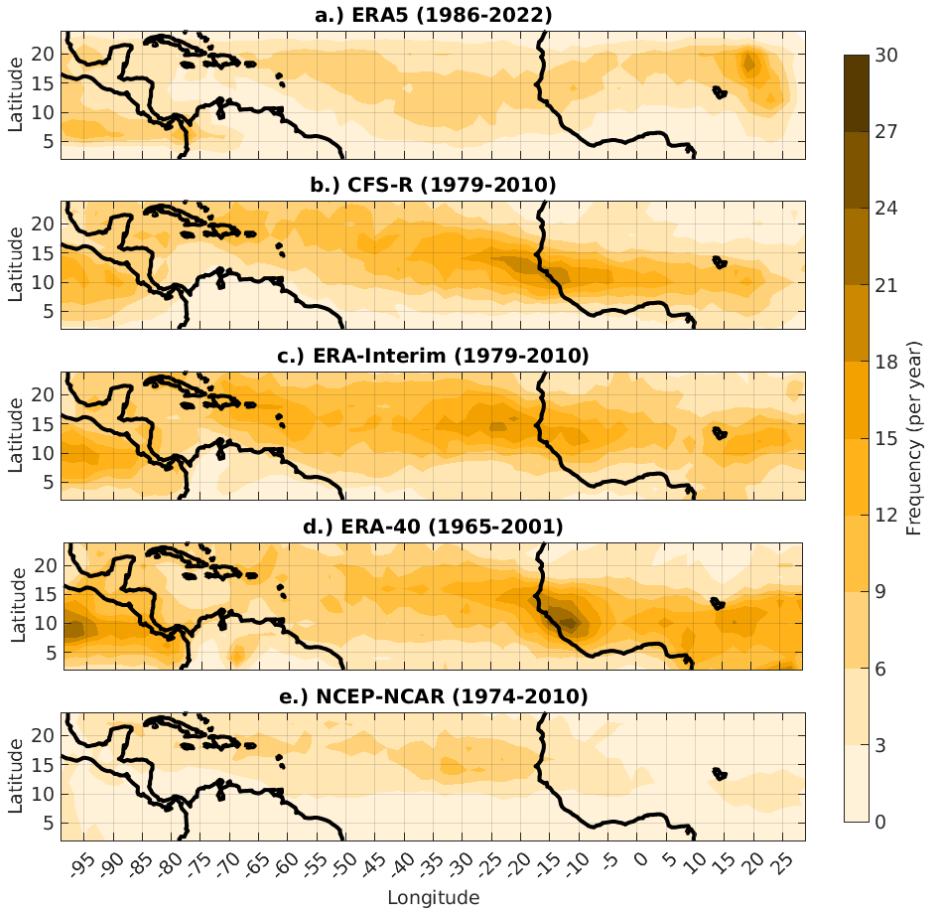

Figure 11: Average May-November TEW track densities at 700 mb for (a) ERA5 from 1986-2022, (b) CFS-R from 1979-2010, (c) ERA-Interim from 1979-2010, (d) ERA-40 from 1965-2001, and (e) NCEP-NCAR from 1974-2010.

Using relative vorticity as a parameter of TEW intensity, the TEWs in Fig. 12 were filtered using an average trough-axis vorticity threshold of 1e-5 s^{-1}. The results from this analysis are presented in Fig. 12. A considerable number of TEWs were removed across Africa and the Atlantic from ERA5 (Fig. 12a), ERA-Interim (Fig. 12c), and NCEP-NCAR (Fig. 12e) while CFS-R (Fig. 12b) and ERA-40 (Fig. 12d) retained a large fraction of their TEWs. Even though TEWs off the west coast of Africa were filtered from ERA-Interim, many East Pacific TEWs remained, showing only a slight decrease of approximately 3 TEWs per year. This was not seen in ERA5 where 6-9 TEWs per year were removed from the Panama Bight region. Overall, across the reanalyses, most of the TEW activity in the East Pacific ITCZ is stronger than the TEW propagating in the Main Development Region (MDR), and NCEP-NCAR dataset continues to be an outlier in terms of TEW frequency.

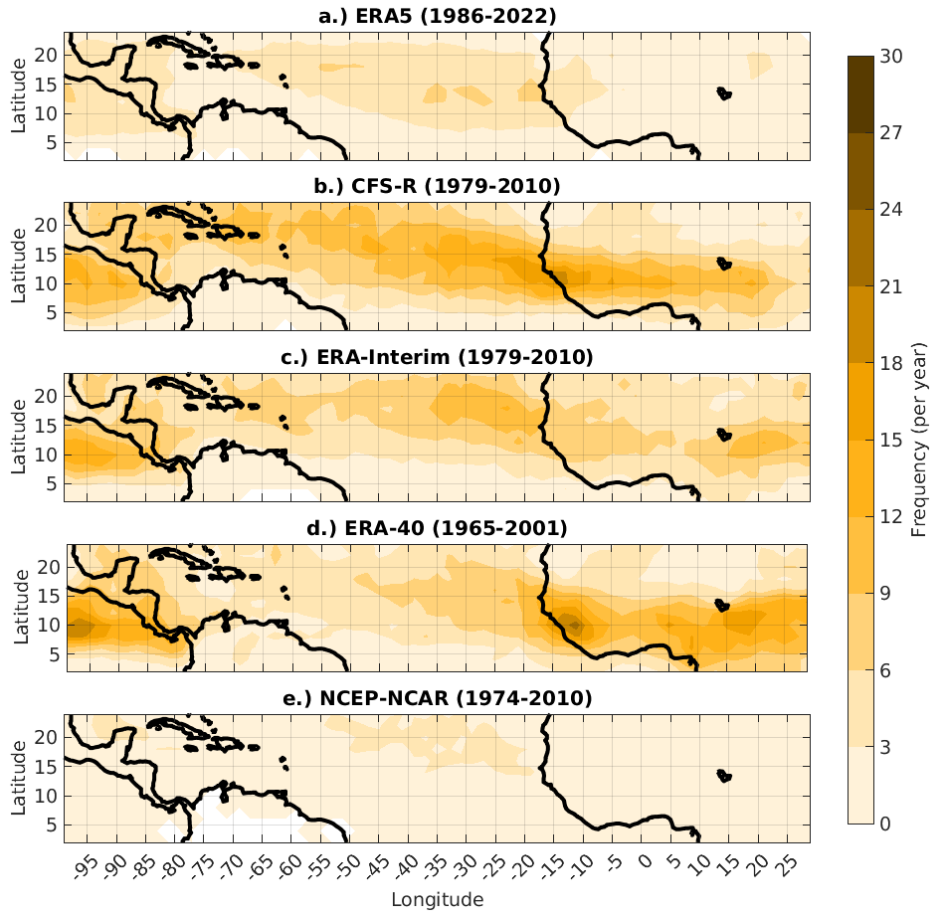

Figure 12: Average May-November TEW filtered track densities at 700 mb for (a) ERA5 from 1986-2022, (b) CFS-R from 1979-2010, (c) ERA-Interim from 1979-2010, (d) ERA-40 from 1965-2001, and (e) NCEP-NCAR from 1974-2010. TEWs are filtered by including only waves that exceed 1e-5 s^{-1}.

Unfiltered and filtered climatological frequencies of TEWs for May-November were also analyzed at 600 hPa and 850 hPa (not shown). The results from those pressure levels did not vary from 700 hPa, except for ERA5 at 850 hPa producing excessive TEW activity over northern Africa around 20°N and in the Bay of Campeche.

3.2.2 African Easterly Jet Latitude

Correlating the average May-November AEJ latitude with the unfiltered track densities of TEWs at 700 hPa yielded intriguing results seen in Fig. 13. Except in the NCEP-NCAR reanalysis (Fig. 13e), statistically significant correlations over northern Africa were nonexistent.

This hints towards TEW propagation and generation over Africa being independent of the AEJ position. This cannot be stated for other regions though.

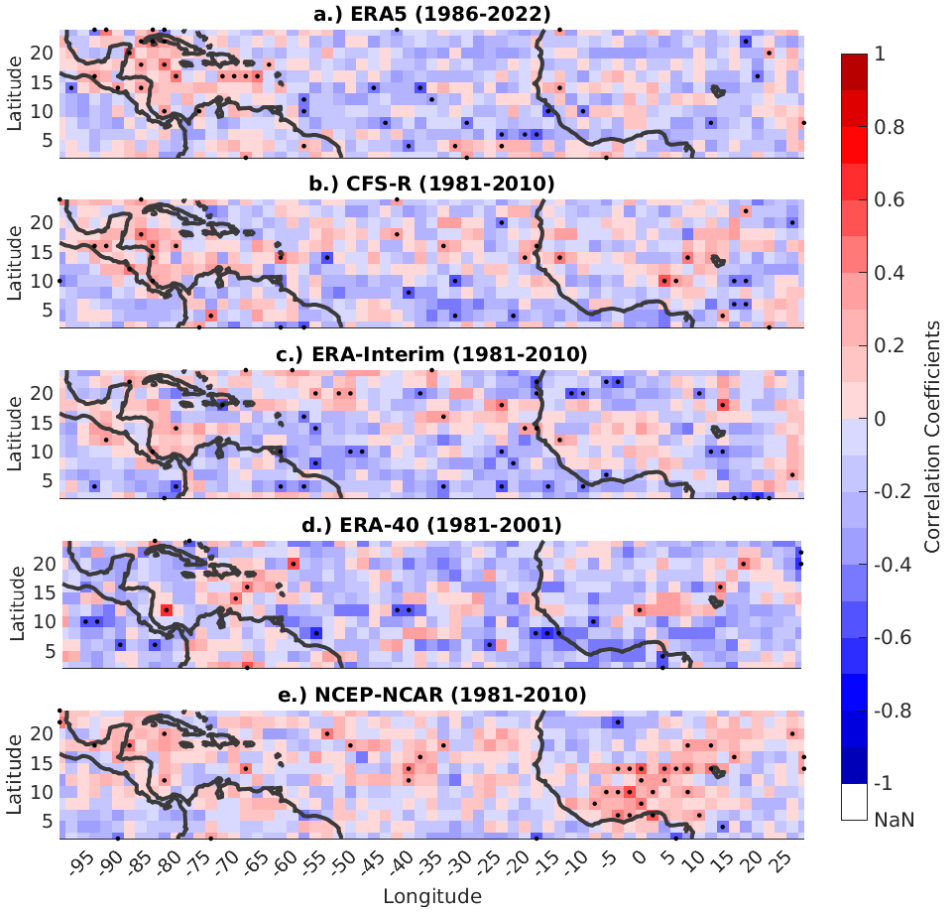

Figure 13: Correlation between average May-November AEJ latitude and the unfiltered May-November TEW track densities at 700 mb for (a) ERA5 from 1986-2022, (b) CFS-R from 1981-2010, (c) ERA-Interim from 1981-2010, (d) ERA-40 from 1981-2001, and (e) NCEP-NCAR from 1981-2010. The black dots represent regions with p-values less than 0.05.

In the western Caribbean Sea, there are regions of positive correlations (i.e., higher AEJ latitude = higher TEW frequency) in ERA5 (Fig. 13a), CFS-R (Fig. 13b), ERA-Interim (Fig. 13c), and NCEP-NCAR. Though the significance of these correlations is not consistent across the reanalyses, it is interesting to see such a distant teleconnection. Looking to the East Pacific, though statistical significance is lacking, there is a band of negative correlations (i.e., lower AEJ latitude = higher TEW frequency) in all datasets except NCEP-NCAR. This dipole structure of TEW correlations between the Caribbean and Pacific sides of Central America is apparent in

ERA5, CFS-R, and ERA-Interim. To potentially explain these teleconnections, correlations between the AEJ latitude and 850 hPa geopotential height, 700 hPa relative humidity, and 200-850 hPa bulk shear were produced. Fig. 14 yielded robust results showing 850 hPa geopotential height and 200-850 hPa bulk shear having statistically significant positive correlations over the East Pacific, indicating that a lower AEJ latitude leads to lower heights and less wind shear over that region. These conditions are favorable for convective organization and TEW generation along with TC intensification. In contrast, there are robust negative correlations for bulk shear over the Caribbean Sea which points to less wind shear with a higher AEJ latitude. This bulk shear teleconnection pattern is nearly identical to what is seen from the El Nino-Southern Oscillation (ENSO) over the Caribbean Sea and East Pacific, and correlating the seasonally averaged AEJ latitude and Oceanic Nino Index (ONI) yielded a statistically significant negative correlation (r = -0.4031).

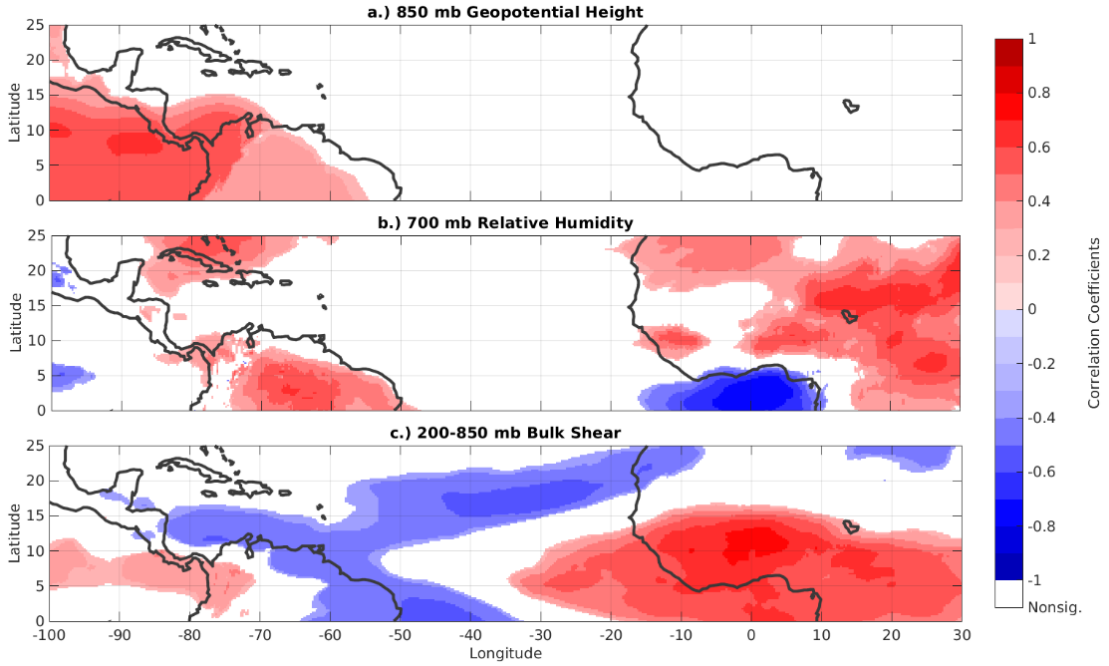

Figure 14: Correlation between average May-November AEJ latitude and (a) 850 hPa geopotential height, (b) 700 hPa relative humidity, and (c) 200-850 hPa bulk shear in ERA5 from 1981-2023. Only regions with p-values less than 0.05 are contoured.

Even though the track and frequency of TEWs over Africa are unaffected, the structure of TEWs are impacted by the latitude of the AEJ. Correlating the probability density functions of TEW amplitudes over Africa and the Atlantic (i.e., 5°N-20°N and 75°W-30°E) with the average

AEJ latitude, Fig. 15 displays a strong signal across all datasets, despite the lack of significance in ERA5 at 850 hPa (Fig. 15a) and ERA-40 at 700 hPa (Fig. 15b) and 600 hPa (Fig. 15c). The AEJ being displaced to the south leads to weaker average TEW amplitudes across all datasets and pressure levels while a northern AEJ produces more amplified TEWs. This pattern cannot be seen when TEWs are analyzed over Central America (i.e., 2°N-20°N and 100°W-75°W), potentially due to the modification of TEWs as they propagate across the Atlantic or recurvature in track away from the region.

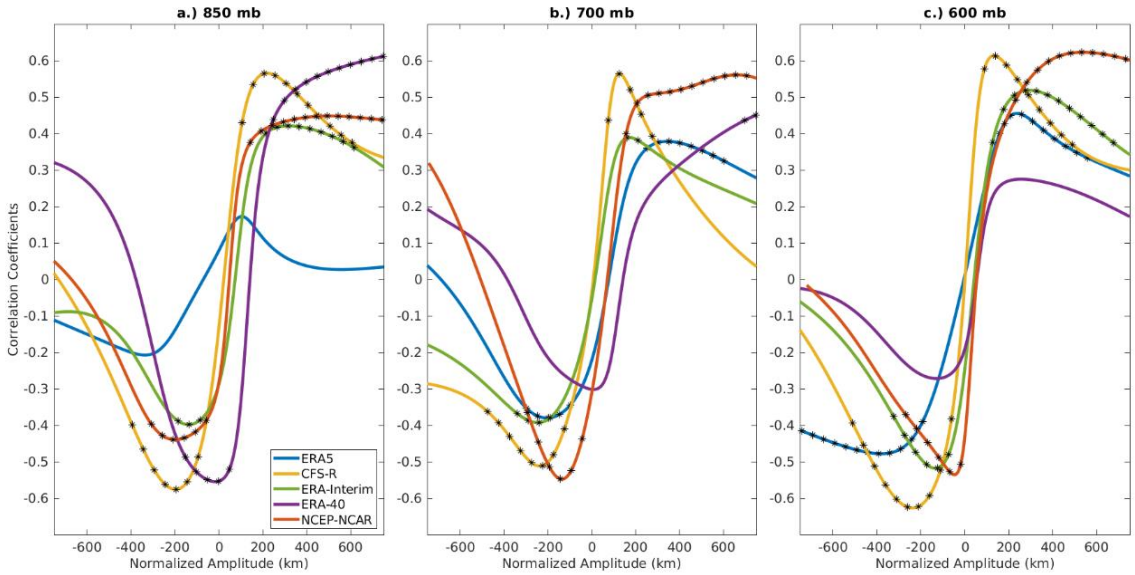

Figure 15: Correlation between average May-November AEJ latitude and the probability density functions of unfiltered TEW average amplitudes over the Atlantic and West Africa for each May-November season normalized using the amplitude at the maximum average probability for each dataset. The black asterisks represent normalized amplitudes with p-values less than 0.05.

Since the amplitude of waves are related to the curvature vorticity in the trough axis, the average areal vorticity of TEWs should match the amplitude correlations. Fig. 16 shows the correlations between the average areal vorticity of TEWs in each reanalysis dataset over Africa and the Atlantic and the average AEJ latitude. Though the correlations are weak at 850 hPa (Fig. 16a) and did not match the amplitude findings, the same pattern can be seen at 700 hPa (Fig. 16b) and 600 hPa (Fig. 16c) with 3-4 of the reanalyses having statistically significant negative correlations at weaker vorticities and positive correlations for stronger vorticities. Therefore, a northern AEJ can lead to TEWs with higher amplitudes and stronger relative vorticities across

Africa and the Atlantic. These TEWs can then strength once they propagate across the Atlantic into the Caribbean Sea where less bulk shear is present.

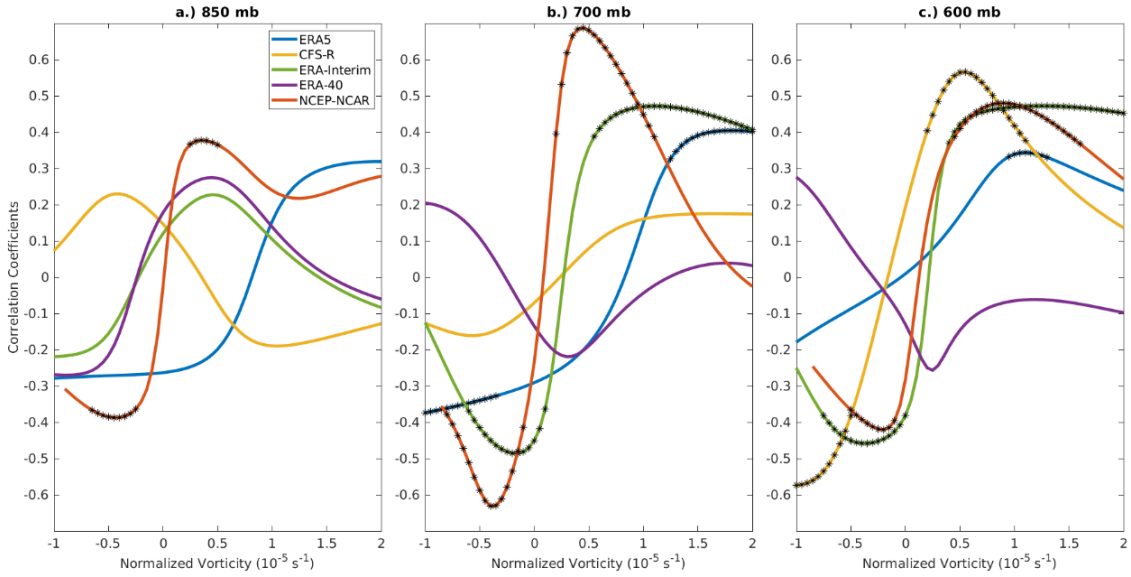

Figure 16: Correlation between average May-November AEJ latitude and the probability density functions of unfiltered TEW average trough-axis relative vorticity over the Atlantic and West Africa for each May-November season normalized using the relative vorticity at the maximum average probability for each dataset. The black asterisks represent normalized relative vorticities with p-values less than 0.05.

3.2.3 African Easterly Jet Strength

Correlating the seasonally averaged AEJ maximum zonal wind speed with the TEW track densities did not produce any robust patterns across the datasets. However, there were some interesting correlations to the environmental parameters. Fig. 17 shows that a stronger AEJ leads to less bulk wind shear over West Africa but drier conditions in the mid-levels. This is contrasted over the subtropical Atlantic with a weaker AEJ having the same environmental impact. However, these conditions counteract each other in terms of TEW intensification which could explain the lack of significant deviations from the average track densities observed over Africa and the Atlantic. The only other statistically significant region is the strong negative correlation seen over the ITCZ region of the East Pacific, translating to a stronger AEJ resulting in higher 700 hPa relative humidity values. Not shown, CFS-R, ERA-40, and NCEP-NCAR did have negative track density correlations over the East Pacific, but consistency in statistical significance was not present.

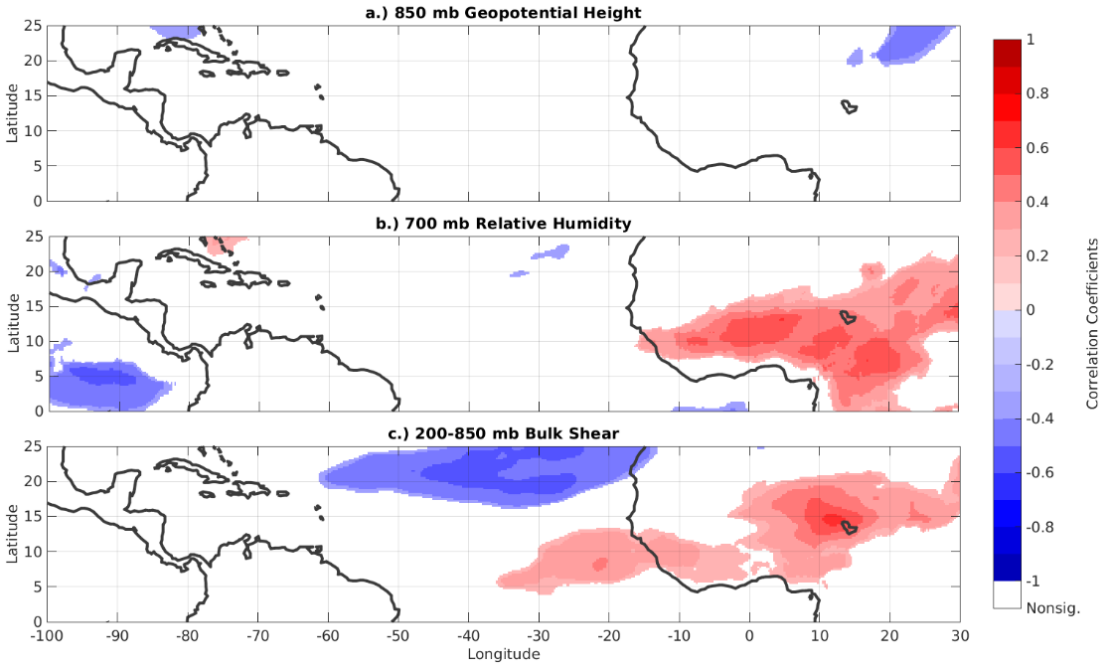

Figure 17: Correlation between average May-November AEJ maximum zonal wind speed and (a) 850 hPa geopotential height, (b) 700 hPa relative humidity, and (c) 200-850 hPa bulk shear in ERA5 from 1981-2023. Only regions with p-values less than 0.05 are contoured.

Similarly, analyzing TEW structures did not yield robust results. The only variable to have the same pattern of correlations is TEW amplitude. Fig. 18 displays the correlations between probability density functions of TEW amplitudes over Central America and the seasonally average of the AEJ maximum zonal wind speed. Though most of the correlations are not statistically significant, there is a consensus across the pressure levels that a weaker AEJ supports shorter TEW amplitudes while a stronger AEJ leads to more amplified TEWs over Central America. These correlations are not reflected in the areal relative vorticity correlations which were seen with the seasonally averaged AEJ latitude (not shown). In addition, this does not align with the findings in Fig. 17 with a weaker AEJ correlated with higher mid-level moisture over the East Pacific, supporting TEW intensification. Overall, May-November averaged AEJ strength does not have a strong impact on the track and structure of TEWs across Africa, the Atlantic, and East Pacific. AEJ strength does influence mid-level relative humidity and 200-850 hPa bulk shear inversely over Africa and the MDR, limiting the impacts of AEJ strength on TEW intensification and cyclogenesis from TEWs.

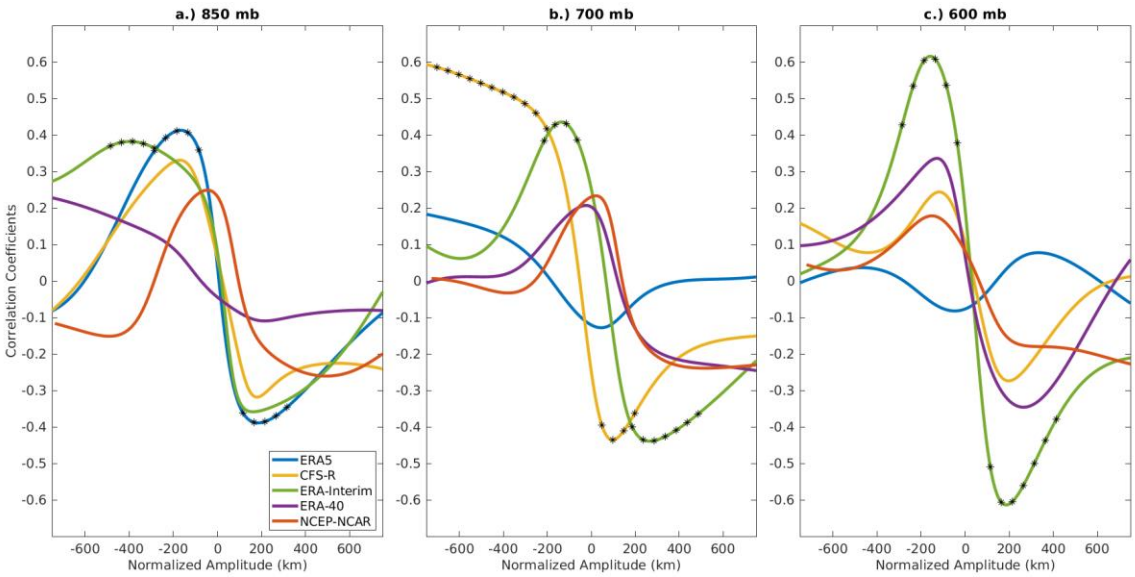

Figure 18: Correlation between average May-November AEJ maximum zonal wind speed and the probability density functions of unfiltered TEW average amplitudes over Central America for each May-November season normalized using the amplitude at the maximum average probability for each dataset. The black asterisks represent amplitudes with p-values less than 0.05.

3.2.4 Central American Monsoon Onset Date

Out of the two monsoonal variations analyzed, the CAM onset dates have the greatest regional correlations with TEW features. Fig. 19 shows the correlations of the CAM onset dates with the filtered climatological frequency of TEWs at 700 hPa. There are two distinct regions of correlations that stand out: northeast of the Leeward Islands and the western Caribbean Sea. Near the Leeward Islands, there are strong negative correlations in CFS-R (Fig. 19b), ERA-Interim (Fig. 19c), and ERA-40 (Fig. 19d) and weaker negative correlations in ERA5 (Fig. 19a) and NCEP-NCAR (Fig. 19e). Negative correlations relate that an earlier CAM onset leads to more frequent TEWs in that region. Stronger TEWs in the MDR region are usually more influenced by the steering of the North Atlantic subtropical high (NASH) as the extent and edge of the ridge determines the location and timing of TEW recurvature over the Atlantic. Therefore, the variations of the NASH could be correlated with the onset of the CAM, indicating a covariation. Moving onto the western Caribbean Sea and southern Gulf of Mexico, statistically significant negative correlations are present in ERA5, CFS-R, and ERA-Interim. These same correlations are seen in NCEP-NCAR but lack significance. A plausible reasoning for these relationships is

the CAM onset influences the intensity of the Central American gyre over the region, leading to local TEW generation on the north and east sides of the gyre.

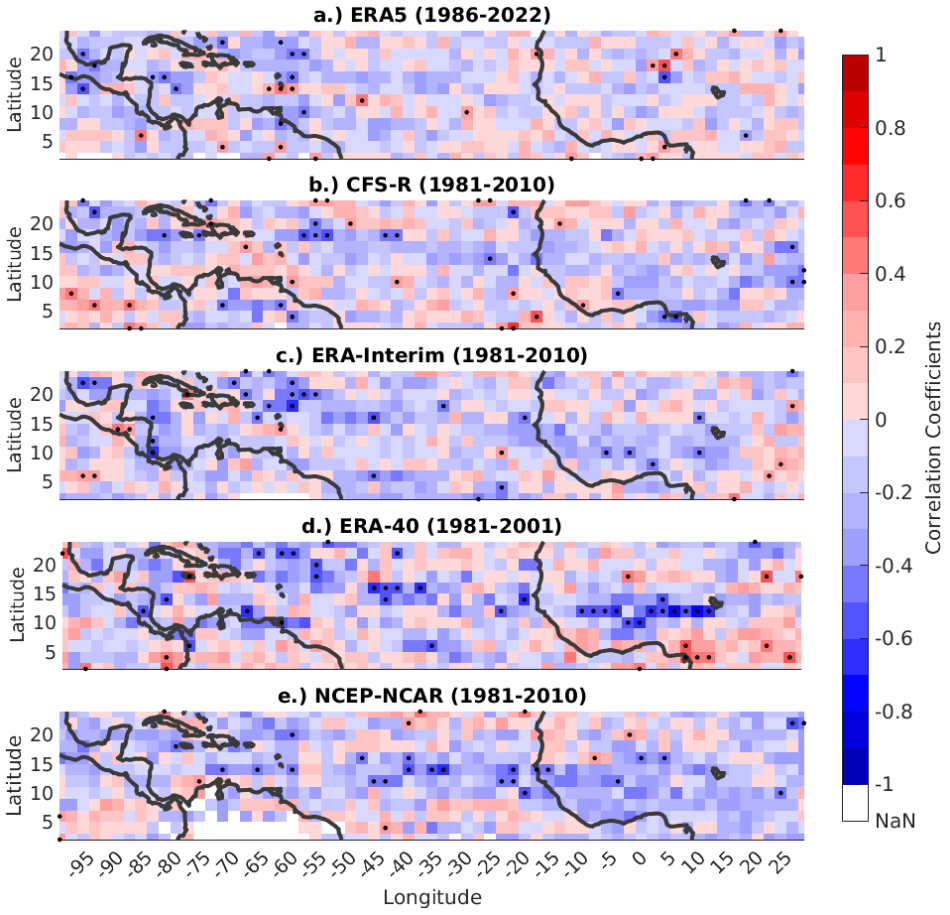

Figure 19: Correlation between CAM onset dates and the filtered May-November TEW track densities at 700 mb for (a) ERA5 from 1986-2022, (b) CFS-R from 1981-2010, (c) ERA-Interim from 1981-2010, (d) ERA-40 from 1981-2001, and (e) NCEP-NCAR from 1981-2010. The black dots represent regions with p-values less than 0.05.

Next, the environmental parameters were correlated with the CAM onset dates and are shown in Fig. 20. The seasonally averaged NASH is influenced by the onset of the CAM with statistically significant positive correlations over much of the Atlantic and Caribbean Sea north of 10°N, translating to an earlier onset with lower 850 hPa geopotential height. The theory about the Central American gyre also appears to be true with robust negative correlations between the CAM onset and 700 hPa relative humidity present over the western Caribbean Sea into the East Pacific. Negative correlations mean that earlier onsets produce higher levels of mid-level

moisture. Looking at 200-850 bulk shear, there are also statistically significant positive relations in the Caribbean Sea, indicating an earlier onset of the CAM is linked with lower wind shear over the region. Therefore, the environment in the western Caribbean is prime for TEW generation and intensification with lower background heights at 850 hPa, higher 700 hPa relative humidity, and lower 200-850 hPa bulk shear when the CAM season starts early. Shifting back to the region northeast of the Leeward Islands, there is also a region of strong negative correlations in terms of 700 hPa relative humidity which, along with the weaker NASH, would support the intensification of recurving TEWs in the MDR.

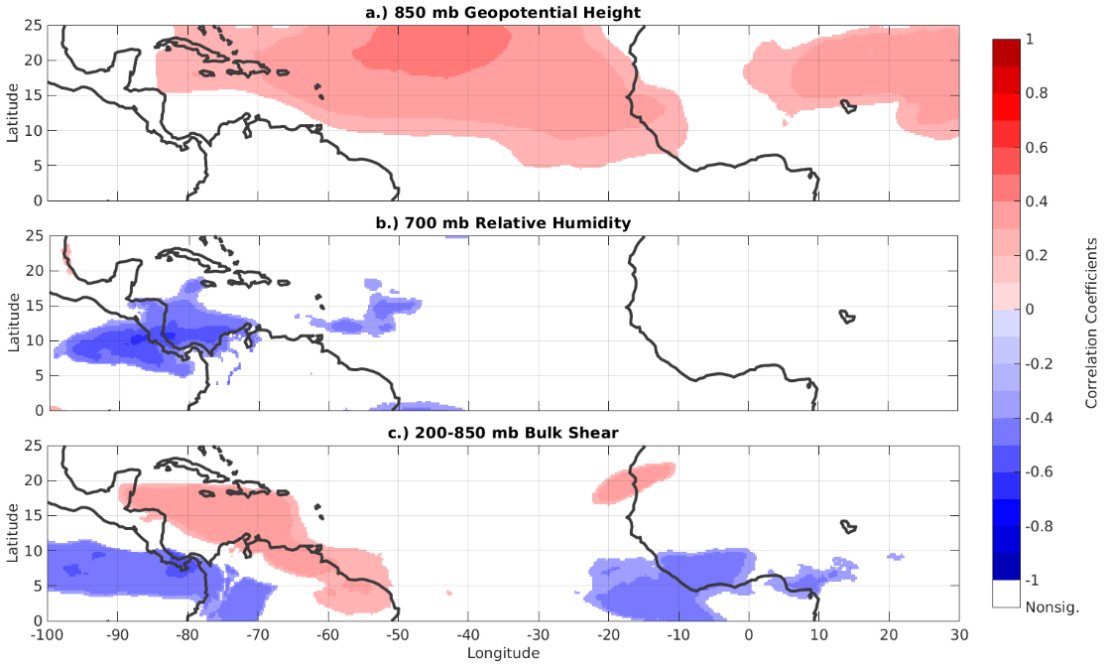

Figure 20: Correlation between the CAM onset date and (a) 850 hPa geopotential height, (b) 700 hPa relative humidity, and (c) 200-850 hPa bulk shear in ERA5 from 1981-2023. Only regions with p-values less than 0.05 are contoured.

Surprisingly though, when examining TEW structures in relation to the CAM onset, no significant pattern arose across the datasets. This means that the CAM does not impact TEW structures the way that the seasonally averaged AEJ latitude did. It's important to note though that the correlations seen in Fig. 15 and Fig. 16 are likely linked to ENSO rather than the AEJ latitude as when correlating the seasonally averaged ONI index from May-November with the variations analyzed, only the AEJ latitude provided a statistically significant correlation. The WAM onset dates were also examined, but no robust correlations could be established in terms of

the seasonal frequency of TEWs or their structures. In addition, the WAM onset dates had little significant impact on the environmental parameters, even over Africa and the MDR.

CHAPTER 4

CONCLUSIONS

In this study, TEWs were simulated by dynamically downscaling a low-resolution reanalysis dataset, and TEW frequency and structure correlations were established with the seasonal AEJ variations and monsoonal onsets.

4.1 Dynamical Downscaling

The RSM-ROMS model was utilized to downscale NCEP R2, and improvements in the simulation of TEW frequency were seen in the RCM with 3-7 more TEWs being generated along the Pacific coast of Central America than what was observed in NCEP R2. Since TEW activity in the East Pacific was nonexistent in NCEP R2, most of these TEWs produced in RSM-ROMS had to form locally in the region. A key difference between RSM-ROMS and NCEP R2 is the presence of barotropic instability near the Panama Bight region. NCEP R2 does not resolve this gradient between 2-4°N near a mid-level jet off the coast of South America while RSM-ROMS can. This region of barotropic instability is crucial in the downshear growth of MCSs into TEWs seen in the region. The cumulus parameterization applied in RSM-ROMS was also influential on TEW generation as seen in RR-RAS and RR-KF2. Using a more convectively allowing parameterization like KF2 yielded more identifiable TEWs at all pressure levels and produced a more realistic Central American gyre when TEWs were present across the Central American model domain. Regardless of parameterization though, the RSM-ROMS model underestimated TEW activity near the equatorial latitudes in the East Pacific that were observed in ERA5 and struggled with accurately simulating terrestrial rainfall, the ITCZ position, and the typical TEW structures that are seen in reanalysis datasets. Overall, simulated TEWs had shorter average wavelengths and weaker average areal vorticity at all pressure levels than what was seen in ERA5 and NCEP R2. This could be partially explained by the highest density of TEWs in the regional model simulations being further north than the more equatorial locations in ERA5. At these higher latitudes, the Rossby radius of deformation is smaller, leading the regional models to possibly produce TEWs of shorter wavelengths, but this argument breaks down with NCEP R2. The probability density functions of wavelength, amplitude, and vorticity in RR-RAS and RR-KF2 were also narrower than what was seen in the reanalyses, showing that RSM-ROMS is

not capturing the variance of TEW structures seen in observations which is a limitation of dynamical downscaling.

In terms of seasonal precipitation, both model simulations underestimated what was observed in ERA5 and IMERGv7, especially over the maritime regions. RR-KF2 was able to match the 10-15% of May-November rainfall attributed to TEWs over Nicaragua seen in ERA5 and IMERGv7 at 600 hPa which was not replicated in RR-RAS. It is important to note though that the seasonal precipitation percentages attributed to TEW activity was highest at 600 mb in RR-RAS and RR-KF2 while at 850 mb in ERA5. This is related to the fact that the model simulations produced more mid-level TEWs than in the low levels which aligns with what was observed in NCEP R2. This shows another flaw of dynamic downscaling. Increasing the spatial resolution of a dataset can improve the simulation of gradients and fluxes but does not remove the inherent biases of the reanalysis used. Shifting to the convective and stratiform precipitation attributed to TEWs, RR-RAS struggled to have TEWs produce widespread convective and stratiform precipitation, limiting to what was observed to over the continent. In RR-KF2, TEWs produced higher seasonal convective and stratiform precipitation percentages than RR-RAS, extending further over the maritime region around Central America, showing a huge improvement between cumulus parameterizations. This could support more downstream TEW development as discussed in Torres et al. (2021) which showed that a stratiform heating profile favors TEW generation. Future work should investigate the profiles of latent heating in RSM-ROMS versus ERA5 to determine why TEW development is favored at 600 hPa in RR-RAS and RR-KF2 rather than at 850 hPa. In addition, enhancements need to be made to RSM-ROMS to reduce the terrestrial rain bias observed to better simulate seasonal TEW rainfall.

4.2 Observational Analysis

The climatology of TEW track densities relied heavily on the reanalysis dataset and its spatial resolution, especially when using an objective algorithm like the one utilized in this study (Belanger et al. 2017). Generally, across the 5 reanalyses analyzed, there are two identifiable local maxima in TEW activity: near the west coast of Africa and the ITCZ region of the East Pacific. Though not seen in NCEP-NCAR, the local generation of TEWs near the Panama Bight region appears in ERA5, ERA-Interim, ERA-40, and CFS-R which is consistent with Rydbeck et al. (2017), Whitaker and Maloney (2020), and Torres et al. (2021). Filtering the TEW track

densities by areal averaged relative vorticity yielded varying results between reanalyses with ERA5, ERA-Interim, and NCEP-NCAR losing a significant number of their TEWs. This issue, again, goes back to the reanalysis used as there are inconsistencies in the models used to produce and assimilate the data along with the lower resolution data being smoothed, removing mesoscale features. Therefore, filtering TEWs by a single threshold across datasets may not be an applicable technique to analyze TEWs, and percentiles may be a more accurate method.

Looking at the correlations between TEW track densities and environmental parameters, the average May-November AEJ latitude and the onset of the CAM produced the most robust results. Both the AEJ latitude and CAM influences the frequency of TEW in the Caribbean Sea through impacting 850 hPa height patterns, 700 hPa relative humidity, and bulk shear in the 200-850 hPa level. A northerly AEJ supports more TEWs in the Caribbean Sea, especially near Central America, as wind shear over the region is lessened due to the higher heights in the East Pacific region, weakening the CLLJ. An early onset of the CAM also supports more TEW activity in the same region as the weaker NASH lessens the CLLJ and wind shear over the Caribbean Sea along with enhance mid-level moisture from the active Central American gyre. These conditions support TEW intensification as these correlations were strongest when using the filtered TEW track densities. Despite these statistically significant correlations, the CAM onset and the latitude of the AEJ are influenced by other climate modes. The seasonally averaged AEJ latitude is negatively correlated with ENSO which is beneficial for seasonal forecasts since ENSO has low variance on higher temporal scales when compared to the AEJ. Additional analysis is needed to determine the extent of the NASH's influence on the CAM system. However, since the onset of the CAM can be determined by May, this parameter can be beneficial in determining where tropical cyclogenesis will be favored during May-November.

Beyond TEW frequency, variations in the AEJ strength and latitude does influence TEW structure over the Atlantic and East Pacific. Even though no robust correlations between TEW frequency and AEJ latitude were established across the reanalyses over Africa and the Atlantic, TEW amplitudes in these regions are highly impacted by the latitude of the AEJ. A northward displacement of the seasonally averaged AEJ supported more amplified TEWs across Africa and the MDR while a southerly AEJ hampered meridional development of TEWs. This correlated to areal averaged relative vorticity as well with a northerly AEJ producing stronger vorticity values

in the trough axis while a southerly AEJ led to weaker TEWs. This was also partially seen with seasonally averaged AEJ maximum zonal wind speed as a stronger AEJ generated stronger TEWs in terms of areal vorticity and weaker TEWs with a weaker AEJ. Therefore, the ideal conditions for TEWs with greater areal vorticity would be a stronger, northerly AEJ which typically occurs when there is above average convection over the Sahel region in the presence of an enhanced Saharan air layer, enhancing the temperature gradient across northern Africa (Bercos-Hickey et al. 2020). The CAM and WAM onsets did not have any pronounced impact on TEW structures that were seen across the reanalyses.

Future work in terms of observational analysis of TEWs should focus on testing these correlations found in this study with alternative tracking methods used to identify TEWs. If these TEW relationships, especially the CAM onset and AEJ latitude/ENSO, can be validated by other tracking techniques, seasonal forecasts of TCs and regional precipitation can be improved as these conditions are easily identifiable by the beginning of the Atlantic hurricane season.

REFERENCES

Agudelo, P. A., C. D. Hoyos, J. A. Curry, and P. J. Webster, 2011: Probabilistic discrimination between large-scale environments of intensifying and decaying African easterly waves. *Climate Dyn.*, **36**, 1379-1401.

Alpert, J., M. Kanamitsu, P. Caplan, J. Sela, and G. White, 1988: Mountain induced gravity wave drag parameterization in the NMC medium-range forecast model. In Conference on Numerical Weather Prediction, 8th, Baltimore, MD. 726-733.

Amador, J. A., 1998: A climatic feature of the tropical Americas: The trade wind easterly jet. *Top. Meteor. Oceanogr.*, **5**, 91–102.

Avila, L. A., and R. J. Pasch, 1992: Atlantic tropical systems of 1991. *Mon. Wea. Rev.*, **120**, 2688–2696.

Belanger, J. I., M. T. Jelinek, and J. A. Curry, 2017: A climatology of easterly waves in the tropical Western Hemisphere. *Geosci. Data J.*, **3**, 40–49, https://doi.org/10.1002/gdj3.40.

Bercos-Hickey, E. and C. M. Patricola, 2025: Drivers of Atlantic Tropical Cyclogenesis: African Easterly Waves and the Environment. *Geophysical Research Letter*, **52**(2), https://doi.org/10.1029/2024GL112002.

Bercos-Hickey, E., T. R. Nathan, and S. Chen, 2020: On the Relationship between the African Easterly Jet, Saharan Mineral Dust Aerosols, and West African Precipitation. *J. Climate*, **33**, 3533–3546, https://doi.org/10.1175/JCLI-D-18-0661.1.

Berry, G., C. Thorncroft, and T. Hewson, 2007: African Easterly Waves during 2004—Analysis Using Objective Techniques. *Mon. Wea. Rev.*, **135**, 1251–1267, https://doi.org/10.1175/MWR3343.1.

Burpee, R. W., 1972: The origin and structure of easterly waves in the lower troposphere of North Africa. *J. Atmos. Sci.*, **29**, 77–90, doi:10.1175/1520-0469(1972)029<0077:TOASOE>2.0.CO;2.

Burpee, R. W., 1974: Characteristics of North African easterly waves during the summers of 1968 and 1969. *J. Atmos. Sci.*, **31**, 1556–1570, doi:10.1175/1520-0469(1974)031<1556:CONAEW>2.0.CO;2.

Carlson, T. N., 1969: Synoptic histories of three African disturbances that developed into Atlantic hurricanes. *Mon. Wea. Rev.*, **97**, 256–275.

Carton, J. A. and B. S. Giese, 2008: A reanalysis of ocean climate using Simple Ocean Data Assimilation (SODA). *Mon. Wea. Rev.*, **136**, 2999–3017, https://doi.org/10.1175/2007MWR1978.1.

Chou, M. D. and K. T. Lee, 1996: Parameterizations for the absorption of solar radiation by water vapor and ozone. *J. Atmos Sci.*, **53**, 1203–1208, https://doi.org/10.1175/15200469(1996)0532.0.co;2.

Chou, M. D. and M. J. Suarez, 1994: An efficient thermal infrared radiation parameterization for use in general circulation models. *NASA Technical Memorandum NASA-TM-104606*, **3**, 98. Retrieved from https://ntrs.nasa.gov/archive/nasa/casi.ntrs.nasa.%20gov/19950009331.pdf.

Cook, K. H. and E. K. Vizy, 2010: Hydrodynamics of the Caribbean low-level jet and its relationship to precipitation. *J. Climate*, **23**, 1477–1494, https://doi.org/10.1175/2009JCLI3210.1.

Dee, D. P., and Coauthors, 2011: The ERA-Interim reanalysis: Configuration and performance of the data assimilation system. *Quart. J. Roy. Meteor. Soc.*, **137**(656), pp.553-597.

Diaz, M., and A. Aiyyer, 2015: Absolute and convective instability of the African easterly jet. *J. Atmos. Sci.*, **72**, 1805–1826, doi:10.1175/JAS-D-14-0128.1.

Dominguez, C., J. M. Done, and C. L. Bruyère, 2020: Easterly wave contributions to seasonal rainfall over the tropical Americas in observations and a regional climate model. *Climate Dyn.*, **54**, 191–209, https://doi.org/10.1007/s00382-019-04996-7.

Ek, M. B., K. E. Mitchell, Y. Lin, E. Rogers, P. Grunmann, V. Koren, G. Gayno, and J. D. Tarpley, 2003: Implementation of Noah land surface model advances in the National Centers for Environmental Prediction operational mesoscale Eta model. *J. Geophys. Res.*, **108**(D22).

Emanuel, K. A., 2022: Tropical cyclone seeds, transition probabilities, and genesis. *J. Climate*, **35**(11), 3557–3566. https://doi.org/10.1175/JCLI-D-21-0922.1.

Ezer, T., H. Arango, and A. F. Shchepetkin, 2002: Developments in terrain-following ocean models: intercomparisons of numerical aspects. *Ocean Modelling*, **4**, 249-267.

Ferreira, R. N., and W. H. Schubert, 1997: Barotropic aspects of ITCZ breakdown. *J. Atmos. Sci.*, **54**, 261–285, https://doi.org/10.1175/1520-0469(1997)054<0261:BAOIB>2.0.CO;2.

Fink, A. H., and A. Reiner, 2003: Spatio-temporal variability of the relation between African Easterly Waves and West African Squall Lines in 1998 and 1999. *J. Geophys. Res.*, **108**, 4332, doi:10.1029/2002JD002816.

Fink, A. H., D. G. Vincent, P. M. Reiner, and P. Speth, 2004: Mean State and Wave Disturbances during Phases I, II, and III of GATE Based on ERA-40. *Mon. Wea. Rev.*, **132**, 1661–1683, https://doi.org/10.1175/1520-0493(2004)132<1661:MSAWDD>2.0.CO;2.

Fuller, R. D., and D. J. Stensrud, 2000: The Relationship between Tropical Easterly Waves and Surges over the Gulf of California during the North American Monsoon. *Mon. Wea. Rev.*, **128**, 2983–2989, https://doi.org/10.1175/1520-0493(2000)128<2983:TRBTEW>2.0.CO;2.

Funk, C., and Coauthors, 2015: The climate hazards infrared precipitation with stations—a new environmental record for monitoring extremes. *Scientific data*, **2**(1), 1-21.

Gray, W. M., 1968: Global View of the Origins of Tropical Disturbances and Storms. *Mon. Wea. Rev.*, **96**, 669-700.

Haidvogel, D. B., H. G. Arango, K. Hedstrom, A. Beckmann, P. Malanotte-Rizzoli, and A. F. Shchepetkin, 2000: Model evaluation experiments in the North Atlantic Basin: Simulations in nonlinear terrain-following coordinates. *Dyn. Atmos. Oceans*, **32**(3), 239–281. https://doi.org/10.1016/s0377-0265(00)00049-x.

Ham, S., and S. Y. Hong, 2013: Sensitivity of simulated intraseasonal oscillation to four convective parameterization schemes in a coupled climate model. *Asia-Pacific J. Atmos. Sci.*, **49**, 483-496.

Ham, S., K. Yoshimura, and H. Li, 2016: Historical dynamical downscaling for East Asia with the atmosphere and ocean coupled regional model. *J. Meteor. Soc. Japan*, **94A**, 199–208. https://doi.org/10.2151/jmsj.2015-046.

He, X., H. Kim, P. E. Kirstetter, K. Yoshimura, E. C. Chang, C. R. Ferguson, J. M. Erlingis, Y. Hong, and T. Oki, 2015: The diurnal cycle of precipitation in regional spectral model simulations over West Africa: sensitivities to resolution and cumulus schemes. *Wea. Forecasting*, **30**(2), 424-445.

Hersbach, H., and Coauthors, 2020: The ERA5 global reanalysis. *Quart. J. Roy. Meteor. Soc.*, **146**(730), 1999-2049.

Hodges, K. I., 1995: Feature Tracking on the Unit Sphere. *Mon. Wea. Rev.*, **123**, 3458–3465, https://doi.org/10.1175/1520-0493(1995)123<3458:FTOTUS>2.0.CO;2.

Hong, S.-Y., and H.-L. Pan, 1996: Nonlocal boundary layer vertical diffusion in a medium-range forecast model. *Mon. Wea. Rev.*, **124**, 2322–2339.

Hsieh, J., and K. H. Cook, 2007: A Study of the Energetics of African Easterly Waves Using a Regional Climate Model. *J. Atmos. Sci.*, **64**, 421–440, https://doi.org/10.1175/JAS3851.1.

Juang, H. M., and M. Kanamitsu, 1994: The NMC nested regional spectral model. *Mon. Wea. Rev.*, **122**, 3–26, https://doi.org/10.1175/ 1520-0493(1994)1222.0.co;2.

Kain, J., and M. Fritsch, 1993: Convective parameterization for mesoscale models: The Kain-Fritsch scheme, *Meteorol. Monogr.*, **24**, 165–170.

Kalnay, E., and Coauthors, 1996: The NCEP/NCAR 40-Year Reanalysis project. *Bull. Amer. Meteor. Soc.*, **77**, 437–471.

Kanamitsu, M., W. Ebisuzaki, J. Woollen, S. Yang, J. J. Hnilo, M. Fiorino, and G. L. Potter, 2002: NCEP–DOE AMIP-II Reanalysis (R-2). *Bull. Amer. Meteor. Soc.*, **83**, 1631–1644, https://doi.org/10.1175/BAMS-83-11-1631.

Kiladis, G. N., C. D. Thorncroft, and N. G. Hall, 2006: Three-dimensional structure and dynamics of African easterly waves. Part I: Observations. *J. Atmos. Sci.*, **63**, 2212–2230.

Ladwig, W. C., and D. J. Stensrud, 2009: Relationship between Tropical Easterly Waves and Precipitation during the North American Monsoon. *J. Climate*, **22**, 258–271, https://doi.org/10.1175/2008JCLI2241.1.

Landsea, C., 1993: A climatology of intense (or major) Atlantic hurricanes. *Mon. Wea. Rev.*, **121**, 1703-1713.

Large, W. G., and J. C. McWilliams, and S. C. Doney, 1994: Oceanic vertical mixing: A review and a model with a nonlocal boundary layer parameterization. *Rev. Geophys.*, **32**(4), 363-403.

Lawton, Q., R. Rios-Berrios, S. J. Majumdar, and W. Downs, 2025: Techniques for the Identification and Modification of Simulated Tropical Waves. *105th AMS Annual Meeting*, New Orleans, LA, Amer. Meteor. Soc., https://ams.confex.com/ams/105ANNUAL/meetingapp.cgi/Paper/455985.

Li, H., M. Kanamitsu, and S. Y. Hong, 2012: California reanalysis downscaling at 10 km using an ocean-atmosphere coupled regional model system. *J. Geophys. Res.*, **117**(D12).

Liebmann, B., and J. Marengo, 2001: Interannual Variability of the Rainy Season and Rainfall in the Brazilian Amazon Basin. *J. Climate*, **14**, 4308–4318, https://doi.org/10.1175/1520-0442(2001)014<4308:IVOTRS>2.0.CO;2.

Lin, Y. L., K. E. Robertson, and C. M. Hill, 2005: Origin and propagation of a disturbance associated with an African easterly wave as a precursor of hurricane Alberto (2000). *Mon. Wea. Rev.*, **133**, 3276–3298, doi:10.1175/MWR3035.1.

McBride, J. L., and R. Zehr, 1981: Observational analysis of tropical cyclone formation. Part II: Comparison of non-developing versus developing systems. *J. Atmos. Sci.*, **38**, 1132–1151.

Mekonnen A., C. D. Thorncroft, and A. R. Aiyyer, 2006: Analysis of convection and its association with African easterly waves. *J. Climate*, 19, 5405–5421, doi:10.1175/JCLI3920.1.

Mellor, G. L., and T. Yamada, 1982: Development of a turbulence closure model for geophysical fluid problems. *Rev. Geophys.*, **20**(4), 851–875.

Misra, V., and S. DiNapoli, 2014: The variability of the Southeast Asian summer monsoon. *Int. J. Climatol.*, **34**(3), 893-901, https://doi.org/10.1002/joc.3735.

Misra, V., C. B. Jayasankar, A. K. Mishra, A. Mitra, and P. Murugavel, 2022: Dynamic downscaling the South Asian Summer Monsoon from a global reanalysis using a regional coupled ocean-atmosphere model. *J. Geophys. Res.*, **127**, e2022JD037490. https://doi.org/10.1029/2022JD037490.

Molinari, J., D. Vollaro, S. Skubis, and M. Dickinson, 2000: Origins and mechanisms of Eastern Pacific Tropical Cyclogenesis: A Case Study. *Mon. Wea. Rev.*, **128**, 125-139.

Moorthi, S., and M. J. Suarez, 1992: Relaxed Arakawa-Schubert. A parameterization of moist convection for general circulation models. *Mon. Wea. Rev.*, **120**, 978–1002, https://doi.org/10.1175/1520-0493(1992)1202.0.co;2.

Peishu, Z., T. Jianping, W. Shuyu, X. Lingyun, Y. Jianwei, Z. Yunqian, N. Xiaorui, and L. Chao, 2017: Dynamical downscaling of regional climate over eastern China using RSM with multiple physics scheme ensembles. *Theor. Appl. Climatol.*, **129**, 1263-1277.

Reed, R. J., D. C. Norquist, and E. E. Recker, 1977: The Structure and Properties of African Wave Disturbances as Observed During Phase III of GATE. *Mon. Wea. Rev.*, **105**, 317–333, https://doi.org/10.1175/1520-0493(1977)105<0317:TSAPOA>2.0.CO;2.

Rydbeck, A. V., E. D. Maloney, and G. J. Alaka, 2017: In Situ Initiation of East Pacific Easterly Waves in a Regional Model. *J. Atmos. Sci.*, **74**, 333–351, https://doi.org/10.1175/JAS-D-16-0124.1.

Saha, S., and Coauthors, 2010: The NCEP Climate Forecast System Reanalysis. *Bull. Amer. Meteor. Soc.*, **91**, 1015–1058, https://doi.org/10.1175/2010BAMS3001.1.

Seo, H., M. Jochum, R. Murtugudde, A. J. Miller, and J. O. Roads, 2008: Precipitation from African Easterly Waves in a Coupled Model of the Tropical Atlantic. *J. Climate*, **21**, 1417–1431, https://doi.org/10.1175/2007JCLI1906.1.

Serra, Y. L., G. N. Kiladis, and K. I. Hodges, 2010: Tracking and mean structure of easterly waves over the intra-Americas sea. *J. Climate*, **23**, 4823–4840, https://doi.org/10.1175/2010JCLI3223.1.

Shchepetkin, A. F., and J. C. McWilliams, 2005: The regional oceanic modeling system (ROMS): A split-explicit, free-surface, topography-following-coordinate oceanic model. *Ocean Modelling*, **9**(4), 347–404. https://doi.org/10.1016/j.ocemod.2004.08.002.

Thorncroft, C. D., and K. I. Hodges, 2001: African Easterly Wave Variability and Its Relationship to Atlantic Tropical Cyclone Activity. *J. Climate*, **14**, 1166–1179, https://doi.org/10.1175/1520-0442(2001)014<1166:AEWVAI>2.0.CO;2.

Thorncroft, C. D., N. M. J. Hall, and G. N. Kiladis, 2008: Three-Dimensional Structure and Dynamics of African Easterly Waves. Part III: Genesis. *J. Atmos. Sci.*, **65**, 3596–3607, doi:10.1175/2008JAS2575.1.

Tiedtke, M., 1983: The sensitivity of the time-mean large-scale flow to cumulus convection in the ECMWF model. In Proceedings of ECMWF Workshop on Convective in Large-scale Models. European Centre for Medium-Range Weather Forecasts, Reading, United Kingdom. 297–316.

Toma, V. E., and P. J. Webster, 2010: Oscillations of the intertropical convergence zone and the genesis of easterly waves. Part I: Diagnostics and theory. *Climate Dyn.*, **34**, pp.587-604.

Torres, V. M., C. D. Thorncroft, and N. M. J. Hall, 2021: Genesis of Easterly Waves over the Tropical Eastern Pacific and the Intra-Americas Sea. *J. Atmos. Sci.*, **78**, 3263–3279, https://doi.org/10.1175/JAS-D-20-0389.1.

Umlauf, L., and H. Burchard, 2003: A generic length-scale equation for geophysical turbulence models. *J. Mar. Res.*, **61**(2):235-65.

Uppala, S. M., and Coauthors, 2005: The ERA-40 re-analysis. *Quart. J. Roy. Meteor. Soc.*, **131**(612), 2961-3012.

Wang, C., and D. B. Enfield, 2001: The tropical western hemisphere warm pool, *Geophys. Res. Lett.*, **28**, 1635 – 1638.

Whitaker, J. W., and E. D. Maloney, 2020: Genesis of an East Pacific easterly wave from a Panama Bight MCS: A case study analysis from June 2012. *J. Atmos. Sci.*, **77**, 3567-3584.

Zhao, Q., and F. H. Carr, 1997: A prognostic cloud scheme for operational NWP models. *Mon. Wea. Rev.*, **125**, 1931-1953.

BIOGRAPHICAL SKETCH

Connor Michael DeLaune was born and raised in Baton Rouge, Louisiana. He attended the University of Louisiana at Monroe (ULM) in northeastern Louisiana where he worked as an undergraduate research assistant under Dr. Kenneth Leppert, studying the differences between developing and non-developing tropical easterly waves. While at ULM, Connor was selected for the prestigious NOAA Ernest F. Hollings Undergraduate Scholarship which allowed him to complete a summer internship at the Pacific Marine Environmental Laboratory in Seattle, Washington, analyzing the seasonal dependence on the changes in sea surface temperatures and salinity from tropical cyclones in the northern Indian Ocean under Dr. Michael McPhaden. After graduating with his Bachelor of Science in Atmospheric Sciences in May 2023, he attended Florida State University (FSU) to earn a Master of Science in Meteorology. During his time at FSU, Connor worked as a teaching assistant where he led introductory meteorology lab courses along with a computations course. The findings from dynamical downscaling portion of this thesis have been submitted to the Journal of Geophysical Research: Atmospheres in hopes of being Connor's first published work.